AGU ADVANCING EARTH AND SPACE SCIENCE

Water Resources Research

RESEARCH ARTICLE
10.1029/2020WR028480

Special Section:
Advances in Remote Sensing, Measurement, and Simulation of Seasonal Snow

Spatial Distribution and Scaling Properties of Lidar-Derived Snow Depth in the Extratropical Andes

Pablo A. Mendoza[1,2], Thomas E. Shaw[2,3], James McPhee[1,2], Keith N. Musselman[4], Jesús Revuelto[5], and Shelley MacDonell[6]

[1]Department of Civil Engineering, Universidad de Chile, Santiago, Chile, [2]Advanced Mining Technology Center (AMTC), Universidad de Chile, Santiago, Chile, [3]Federal Institute for Forest, Snow and Landscape Research (WSL), Birmensdorf, Switzerland, [4]Institute of Arctic and Alpine Research, University of Colorado Boulder, Boulder, CO, USA, [5]Pyrenean Institute of Ecology, CSIC, Zaragoza, Spain, [6]Centre for Advanced Studies in Arid Zones (CEAZA), La Serena, Chile

Abstract We characterize elevational gradients, probability distributions, and scaling patterns of lidar-derived snow depth at the hillslope scale along the extratropical Andes. Specifically, we analyze snow depth maps acquired near the date of maximum accumulation in 2018 at three experimental sites: (i) the Tascadero catchment (31.26°S, 3,270–3,790 m), (ii) the Las Bayas catchment (33.31°S, 3,218–4,022 m); and (iii) the Valle Hermoso (VH) catchment (36.91°S, 1,449–2,563 m). We examine two subdomains in the latter site: one with (VH West) and one without (VH East) shrub cover. The comparison across sites reveals that elevational gradients are site-dependent, and that the gamma and normal distributions are more robust than the lognormal function to characterize the spatial variability of snow depth. Multiscale behavior in snow depth is obtained in all sites, with up to three fractal regimes, and the magnitude of primary scale breaks is found to be related to the mean separation distance between local snow depth peaks. The differences in snow depth fractal parameters between VH West—the only vegetated subdomain—and the remaining sites suggest that local topographic and land cover properties are dominant controls on the spatial structure of snow, rather than average hydroclimatic conditions. Overall, the results presented here provide, for the first time, insights into the spatial structure of snow depth along the extratropical Andes Cordillera, showing notable similarities with other mountain regions in the Northern Hemisphere and providing guidance for future snow studies.

Key Points:
- We present the first analysis of snow depth distribution in the extratropical Andes using high-resolution lidar measurements
- Multiscale behavior in snow depth is found, and fractal parameters depend on local topography and vegetation rather than climate
- The magnitudes of scale break lengths are related to the mean separation distance between local snow depth peaks

Supporting Information:
- Supporting Information S1

Correspondence to:
P. A. Mendoza,
pamendoz@uchile.cl

Citation:
Mendoza, P. A., Shaw, T. E., McPhee, J., Musselman, K. N., Revuelto, J., & MacDonell, S. (2020). Spatial distribution and scaling properties of lidar-derived snow depth in the extratropical Andes. *Water Resources Research*, *56*, e2020WR028480. https://doi.org/10.1029/2020WR028480

Received 28 JUL 2020
Accepted 10 NOV 2020
Accepted article online 17 NOV 2020

1. Introduction

1.1. Snow in the Extratropical Andes Cordillera

In the semiarid extratropical Andes Cordillera, the seasonal snowpack acts as a natural reservoir, releasing spring snowmelt that accounts for more than 60% of the total annual streamflow (Masiokas et al., 2006) and sustains multiple productive uses, population needs (Mendoza et al., 2014), and unique ecosystems (Cornwell et al., 2016; Masiokas et al., 2020). Hence, understanding the spatial variability of snow depth and snow water equivalent (SWE) in this domain, and possible connections with landscape, vegetation, and meteorological conditions, is critical to improve the spatial configuration of physically based models and contribute toward a better predictability of snowmelt timing and volume (e.g., Freudiger et al., 2017). This is relevant not only for reliable streamflow predictions but also for future water resources planning and management considering projected climate change impacts in this region (e.g., Bozkurt et al., 2018).

The characterization of snow depth and SWE spatial variability along the extratropical Andes Cordillera has been historically challenged by data limitations, since only a few snow courses and automatic stations exist. In spite of this, several studies have aimed to portray the spatial variability of snow depth and SWE in the Andes using in situ measurements, remote sensing products, and/or numerical models. The first efforts to analyze the spatiotemporal behavior of snow cover were conducted by the Chilean Directorate of Water Resources (Escobar & Anabalón, 1991) through the installation of 27 snow courses between 30.2–53.1°S, with elevations spanning 700–4,200 m a.s.l. The information provided by these snow courses was ultimately used to estimate snow line elevations and snow density values to be used for seasonal snowmelt forecasting. Gascoin et al. (2013) produced a 90-m resolution snow data set through the combination of meteorological

observations and SnowModel (Liston & Elder, 2006) in the Huasco River headwaters (northern Chile), demonstrating the need for explicit representation of wind transport to reproduce observed fractional snow covered area (fSCA). Ayala et al. (2014) documented a data set of spatially distributed SWE for the semiarid Andes—obtained from manual point measurements in three headwater catchments—finding altitudinal gradients and a strong relationship between snow distribution and the maximum upwind slope (MUS) parameter above 3,000 m a.s.l. Cornwell et al. (2016) provided a 500-m resolution SWE reconstruction—developed with in situ measurements, an energy balance model and MODIS imagery—for an Andean domain spanning central Chile and Argentina (27–38°S) during 2001–2014. Cortés et al. (2016) presented a SWE product for the Juncal River basin for the period 1985–2015 at a 90-m resolution, from the combination of reanalysis fields, Landsat imagery, land surface modeling, and data assimilation. This product was expanded by Cortés and Margulis (2017) to the extratropical Andes between 27° and 37°S using the same approach to generate a SWE reanalysis data set with a 180-m horizontal resolution. Mernild et al. (2017) combined the MERRA atmospheric reanalysis and SnowModel (Liston & Elder, 2006) to produce a 4-km resolution snow simulation over the entire Andes Range (period 1979–2014), finding spatially variable trends in snow cover days and SWE along the domain analyzed.

Table 1 summarizes these historical efforts to describe the spatial variability of SWE or snow depth, which differ in terms of geographic domain, environment, variables examined, spatial scale and analysis period. Although these studies have provided tremendous insights into the spatiotemporal snowpack patterns along the extratropical Andes at the watershed and regional scales, very little is known in this domain about the spatial structure of snow depth or SWE and driving physical processes below the hillslope scale (i.e., 1–100 m as defined by Clark et al., 2011). While Ayala et al. (2014) provided analyses based on a rich database of survey measurements collected on many hillslopes, the average spacing (as defined by Blöschl, 1999) between observations was larger than 60 m. A recent study by Shaw et al. (2020) reported the first data set with point measurements below 1-m spacing for a 0.74-km^2 subdomain in Central Chile, acquired with light detection and ranging (lidar) technology. Nevertheless, no descriptions of snow depth spatial structure or probabilistic distribution have been provided for the extratropical Andes to date, a gap that we seek to fill.

1.2. Advances in Understanding Snow Variability With Lidar Technology

In other mountain regions of the world, lidar technology has demonstrated its usefulness to characterize the spatial and/or temporal variability of snow depth (e.g., Broxton et al., 2015; Currier et al., 2019; Currier & Lundquist, 2018; Grünewald et al., 2010; Kirchner et al., 2014; Revuelto et al., 2014; Schirmer et al., 2011). A key advantage over manual measurements is the capability to provide unbiased samples of millions of snow depth observations in a short period of time (Currier et al., 2019; Deems et al., 2013; Painter et al., 2016). Additionally, the potential of lidar scanning systems for snow hydrology has been demonstrated for myriad applications, including process-based model evaluation (e.g., Broxton et al., 2015; Musselman et al., 2015), validation of large-scale, satellite-derived snow products (Deschamps-Berger et al., 2020; Shaw et al., 2020), development of statistical models for the spatial prediction of snow depth (e.g., Grünewald et al., 2013; Helbig et al., 2015; Revuelto et al., 2014; Skaugen & Melvold, 2019), data assimilation (Hedrick et al., 2018), and avalanche control and prediction (Deems et al., 2015).

Lidar-derived snow depth maps have provided transformative insights into the statistical distribution (e.g., López-Moreno et al., 2015) and scaling patterns (e.g., Deems et al., 2008) of snow in mountain domains. Additionally, the utility of lidar measurements to inform the spatial configuration of distributed snowmelt models has been broadly recognized. For example, large-scale models may involve implicit representations of subgrid variability, for which parameterizations for the fractional snow covered area and the average snow depth or SWE need to be developed (Clark et al., 2011). One approach is to fit parametric probability density functions (PDFs) to maximum accumulation SWE or even snow depth observations (e.g., Liston, 2004), considering that snow depth is much more variable in space than snow density (Donald et al., 1995; López-Moreno et al., 2013). Early spatial distribution assessments used in situ measurements to test the suitability of lognormal (e.g., Donald et al., 1995) and gamma (e.g., Kuchment & Gelfan, 1996) distributions, transitioning through a mixture of remotely sensed and manual measurements (Marchand & Killingtveit, 2005). Lidar technology has transformed the ability to identify appropriate parametric functions and assess how the optimal distributions vary with spatial extent. For example, Helbig et al. (2015) examined the spatial

Water Resources Research

10.1029/2020WR028480

Table 1
Studies Analyzing the Spatial Variability of Snow Depth or SWE Across the Extratropical Andes Cordillera

Reference	Domain	Environment	Variable analyzed (data source)	Spatial scale (m)	Time period	Main findings on spatial distribution
Escobar & Anabalón (1991)	30.3–53.18°S	Snow courses located at different slope orientations, elevations and hydroclimatic conditions	Snow depth and snow l ine elevation	300–500	1960–1990, more than one observation per month	Latitudinal gradients of snow line elevation. Latitudinal and temporal gradients of snow density.
Gascoin et al. (2013)	29°S, 70°W	Semiarid Alpine	SWE	90	Winter season 2008	Wind patterns are key drivers for snow redistribution. Blowing snow sublimation accounting for 18% of ablation.
Ayala et al. (2014)	32.4–34.0°S	Hillslope 2,200–3,800 (m a.s.l). Mostly unvegetated with few low shrubs and cushion plants	SWE (Hillslope transects)	60–197	2011 to end of accumulation season	Logarithmic trend with respect to elevation from 2,200 to 3,000 (m. a.s.l.). North facing slopes show 25% less snow depth.
Cornwell et al. (2016)	27–38°S	From bare soil (north) to forested regions (south)	SWE (Energy balance reconstruction and validated with observations)	500	2001–2014 (15 August to 15 January, daily)	Strong influence of latitude, elevation and continental divide. Different behavior in the west/east sides of the Andes.
Cortés et al. (2016)	33°S	Semiarid Alpine	SWE	90	1985–2015	High interannual variability in peak SWE fields, explained by ENSO phases.
Cortés and Margulis (2017)	27–37°S	Extratropical Alpine	SWE	180	1984–2015	Same as above for a larger domain. Significant variability of SWE with latitude. High contrast between windward and leeward domains.
Mernild et al. (2017)	The entire Andes range (11.8°N to 53.8°S)	All types (4–6,293 m a.s.l.)	SWE	4,000	1979–2014	Spatial variability of temporal trends in SWE and snow cover extent with latitude and elevation.
Shaw et al. (2020)	33.4°S, 69.9°W	Extratropical Alpine	Snow depth	4	September 2017	Strong relation of snow depth to elevation, northness and slope exposure.
This study	Four hillslope-scale domains along 31–37°S	Semiarid alpine and subalpine	Snow depth	1	Winter 2018 (August–October)	Lognormal distributions are outperformed at the hillslope scale. Multiscale behavior is observed, with scale break lengths that depend on land cover type rather than climate. Scale breaks are similar to distance between local peaks in snow depth.

distribution of snow depth at sites in eastern Switzerland and the Spanish Pyrenees, finding that gamma distributions work well in small domains, while normal distributions are as good or even better in larger areas (>500 m). More recently, Skaugen and Melvold (2019) found that gamma distributions provide better representations of snow depth compared to normal and lognormal distributions at Hardangervidda (southern Norway), while He et al. (2019) demonstrated the suitability of normal distributions in forested sites using airborne lidar scanning (ALS) measurements in southeastern Wyoming.

Lidar-based variogram analysis can be used to inform the spatial scales needed in high-resolution (tens to hundreds of meters) physically based models (e.g., Essery et al., 1999; Liston & Elder, 2006), based on the identification of regions where snow shows fractal scaling (i.e., scale invariant) behavior and the limits (i.e., scale breaks) between those regions. Moreover, these results can help to design predictor variables in statistical models for snow depth (Grünewald et al., 2013). Deems et al. (2006) and Trujillo et al. (2007) analyzed ALS data sets acquired near the date of maximum snow accumulation in forested sites at Colorado (USA), finding two fractal regimes separated by scale breaks of the order of tens of meters. A short-range fractal behavior up to similar scale break lengths has been also found in the Swiss Alps—in ice free (Mott et al., 2011; Schirmer & Lehning, 2011) and glaciated sites (Clemenzi et al., 2018) –, the Ötztal Alps, Austria (Helfricht et al., 2014), and the Spanish Pyrenees (Mendoza, Musselman, et al., 2020), reaffirming earlier findings on the scale-invariant behavior of snow depth based on manual measurements (Arnold & Rees, 2003; Kuchment & Gelfan, 2007; Shook & Gray, 1996). Discrepancies in scale break lengths among studies have been attributed to site characteristics (e.g., type of vegetation, bare ground or ice topography, and exposure to wind) and interactions between these features with snowpack and meteorological variables (Trujillo et al., 2007). Recently, Mendoza, Musselman, et al. (2020) analyzed 24 lidar-derived snow depth maps acquired during six consecutive snow seasons (2011–2017) in a subalpine catchment, finding possible connections between scale break lengths and the optimal search distances used to derive predictors for snow depth, such as the Topographic Position Index (TPI) and the MUS parameter. Despite the fact that the aforementioned studies examined the spatial organization of snow in mountain areas with different hydroclimates and landscape characteristics, to our knowledge, no such study has explored this behavior within the Andes range.

1.3. Scope and Goals

This study sheds light on the spatial distribution, statistical properties, and spatial patterns of snow depth at the hillslope scale across four domains in the extratropical Andes, complementing a large body of work that, so far, has been developed predominantly in a myriad of mountain ranges in the Northern Hemisphere (e.g., Arnold & Rees, 2003; Clark et al., 2011; Clemenzi et al., 2018; Deems et al., 2006; Donald et al., 1995; Grünewald et al., 2014; Helbig et al., 2015; Helfricht et al., 2014; Kuchment & Gelfan, 1996, 2007; Melvold & Skaugen, 2013; Mendoza, Musselman, et al., 2020; Mott et al., 2011; Schirmer et al., 2011; Shook & Gray, 1996; Skaugen & Melvold, 2019). Specifically, we analyze 1-m resolution snow depth maps derived from terrestrial laser scanning (TLS) campaigns conducted at four hillslope sites located in the headwaters of three catchments with varying hydroclimate and landscape properties. All data sets have been acquired near maximum snow accumulation dates in 2018 and are examined in terms of (i) spatial distribution and statistical properties, (ii) scaling regimes, and (iii) possible connections with snow depth transect properties. The results presented here bring new knowledge for mountain water resources in the Andes Cordillera: some of them confirm earlier findings on snow depth distributions and scaling behavior, and others provide new insights that pave the way for research opportunities in mountain environments across the globe.

2. Study Domain and Data

2.1. Site Descriptions

We examine three subdomains with distributed snow depth observations across a range of hydroclimatic conditions along the Chilean extratropical Andes (Figure 1a). The analyzed subdomains are, from north to south, as follows: (i) the Tascadero catchment (31.26°S, 70.53°W, 3,270–3,790 m), (ii) the Las Bayas experimental catchment (33.31°S, 70.25°W, 3,218–4,022 m); and (iii) the Valle Hermoso (VH) catchment (36.91°S, 71.40°W, 1,449–2,563 m). These sites are located in the headwaters of three major basins that provide freshwater for irrigation, industry, and mining (among other purposes) in Central Chile (Figure 1b). Site characteristics and lidar acquisition information are provided here and the details of lidar data processing are described in section 2.3.

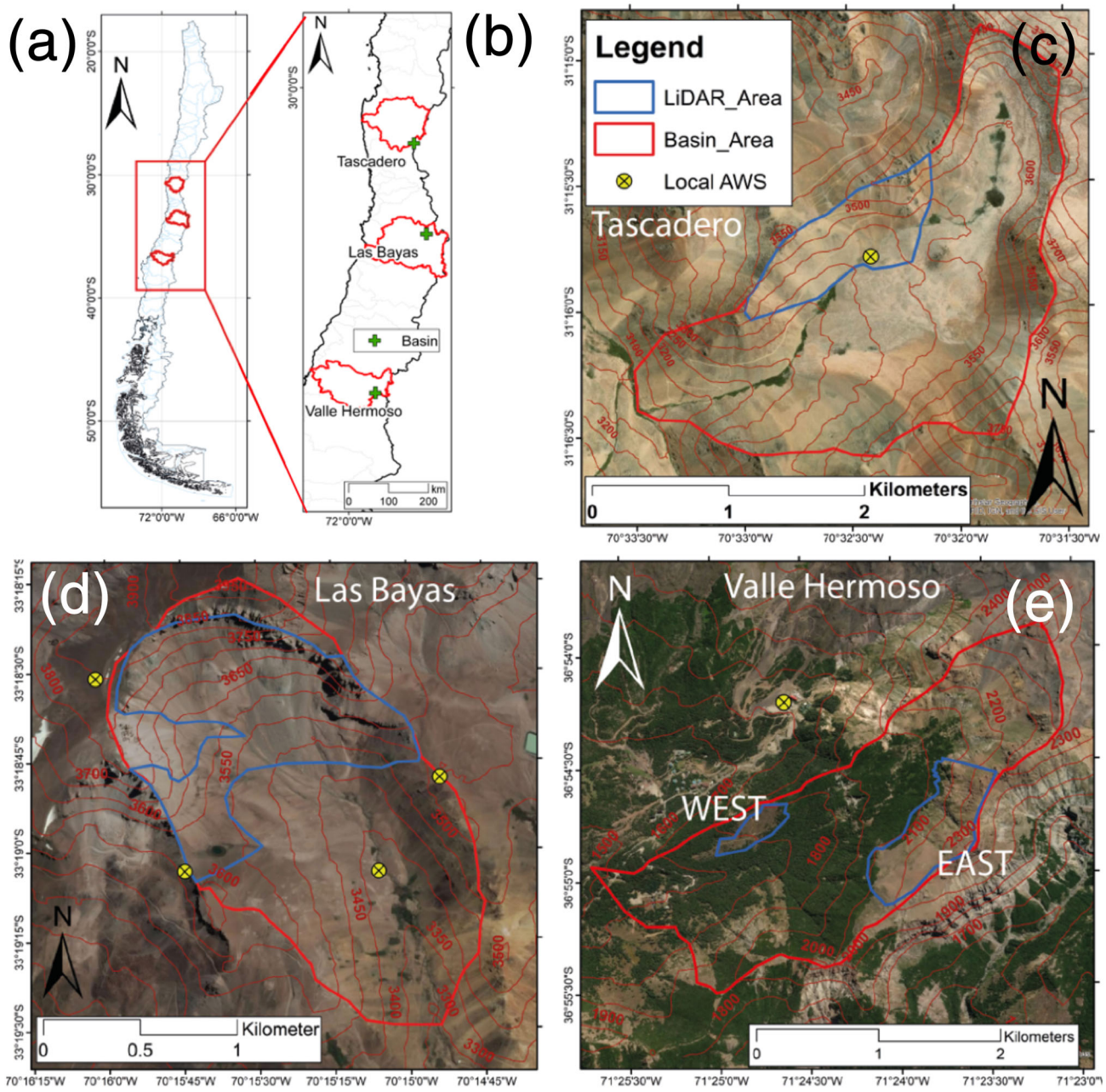

Figure 1. (a) Scanning sites used in this study and their position in the Andes of Chile. The locations of individual sites Tascadero (c), Las Bayas (d) and Valle Hermoso (e) are given in panel (b). Panels (c)–(e) show catchment boundaries in red, scan domains in blue, and local AWS locations are represented by yellow markers. The West and East domains for Valle Hermoso are also displayed (e).

The Tascadero catchment is located within the semiarid region of Coquimbo, ~100 km from the coast, covering an area of ~4 km^2 and oriented southwest (Figure 1c). The site has been the focus of lidar-based research on the application of snow fences to accumulate snow and minimize sublimation losses (Antonissen, 2018), and the original scanning area has been extended for this work to a southeast facing slope with a total area of 0.68 km^2 (17% of the total basin). The second site examined is the upper part of the Las Bayas catchment (Figure 1d), which is oriented southeast and spans an area of ~2.4 km^2 with an average slope of 20°. The catchment is situated at the northeast extent of the Farellones district, and the lidar scan area is 1.01 km^2 (42% of the total basin). The third subdomain of interest, the southwest facing Valle Hermoso catchment, is situated 70 km southeast of the city of Chillán, and spans an area of ~4.5 km^2 (Figure 1e). Since most of

Table 2
Characteristics of the Four Study Sites

Location	Area (km^2)	Elevation (m a.s.l.)	Aridity index (PET/P)	Mean winter precipitation (mm)	Mean winter temperature (°C)	Description
Tascadero	0.68	3,380–3,700	4.7	389	−0.92	Nonvegetated, arid environment
Las Bayas	1.01	3,440–4,070	2.2	518	−0.89	Nonvegetated, semiarid environment
VH West	0.34	1,650–1,845	0.4	2,438	1.74	Sloped terrain that combines shrublands, clearings and a few trees
VH East	0.57	2,020–2,360	0.4	2,438	1.74	Nonvegetated, rocky terrain above treeline of catchment

Note. Hydrometeorological variables correspond to the period 1979–2018, derived from the basin statistics of the CR2MET data set (DGA, 2017). PET and P denote mean annual values of potential evapotranspiration and precipitation, respectively.

this area is covered by dense Nothofagus woodland below the treeline at ~2,080 m a.s.l. (Huerta et al., 2019), we examine two subzones: (i) VH West, whose area is 0.34 km^2 (7.5% of the total basin), and (ii) VH East, which covers 0.57 km^2 (12.5% of the total basin).

The selected sites enable the comparison of snow depth scaling behaviors based on climatic and physiographic differences (see Table 2 for details). Mean annual and winter precipitation amounts increase from north to south. Tascadero, Las Bayas, and VH East are unvegetated alpine sites, while VH West is a subalpine environment that combines shrublands, clearings, and some trees (see Figure S1 in the supporting information). Hence, possible differences in snow depth distribution among Andean sites can be examined in terms of hydroclimate, land cover type, and topographic features such as slope and orientation.

2.2. Meteorological Observations

We complement our variogram analyses through the examination of wind speed and direction measurements acquired from AWSs located in our study domains (Figure 1). The Tascadero weather station (31.26°S, 70.54°W, 3,427 m a.s.l.) is managed by the Centro de Estudios Avanzados en Zonas Áridas (CEAZA), and is located inside the Tascadero study catchment, south from the scanning area (Figure 1c). The Las Bayas experimental catchment has the largest number of automatic weather stations that include wind measurements, with four stations distributed across this subdomain (Figure 1d). The Termas de Chillán station—located north from the Valle Hermoso experimental catchment—is operated by Dirección Meteorológica de Chile (36.9°S, 71.41°W, 1,708 m a.s.l.), and is the closest weather station for this area (Figure 1e). Figure 2 displays wind roses for the three days preceding lidar scans, considering only wind speeds >4 m s^{-1} (following Li & Pomeroy, 1997).

2.3. Lidar

In this study, we adopt the same processing steps at all sites to derive snow depth maps from terrestrial lidar scans. Lidar measurements for snow-covered conditions were conducted on 4 September, 9 August, and 25 October 2018 in Tascadero, Las Bayas and Valle Hermoso, respectively. Each data acquisition was conducted using a Riegl VZ6000 long-range scanner on dates with and without snow, using an angular resolution of 0.01° and equating to a mean point density of ~18 p/m^2 at a 1,000-m distance from the scanner. The scanner operates at a near-infrared wavelength (1,064 nm), increasing range and reflectivity and making it highly suitable for monitoring snow and ice in mountain environments (Deems et al., 2013; Fischer et al., 2016; Shaw et al., 2020). The location of the scanner at each date was measured using a Trimble R4 Real Time Kinematic (RTK) point, providing an absolute position uncertainty of 0.01 and 0.03 m in the horizontal and vertical directions, respectively. We processed each individual point cloud using Riegl Riscan Pro V. 2.5.1, following a manual point-to-point feature matching to coarsely align the cloud and a subsequent iterative cloud matching algorithm (Chunhai Xu et al., 2018) for precise alignment of snow free, stable terrain. Errors of the iterative process were between 0.02–0.04 m, indicating a successful cloud matching result.

We applied an octree filter for point decomposition, and rasterized the individual point clouds at a 1-m horizontal resolution using the CloudCompare software. The difference between individually rasterized digital elevation models (DEMs) with and without snow provides a snow depth map for each site. Quadratic errors of point matching (RiScan) and standard deviation of vertical differences over snow free terrain (that should be equal to zero) provide a total error estimate of 0.04, 0.09, 0.10, and 0.13 m for Tascadero, Las Bayas, VH

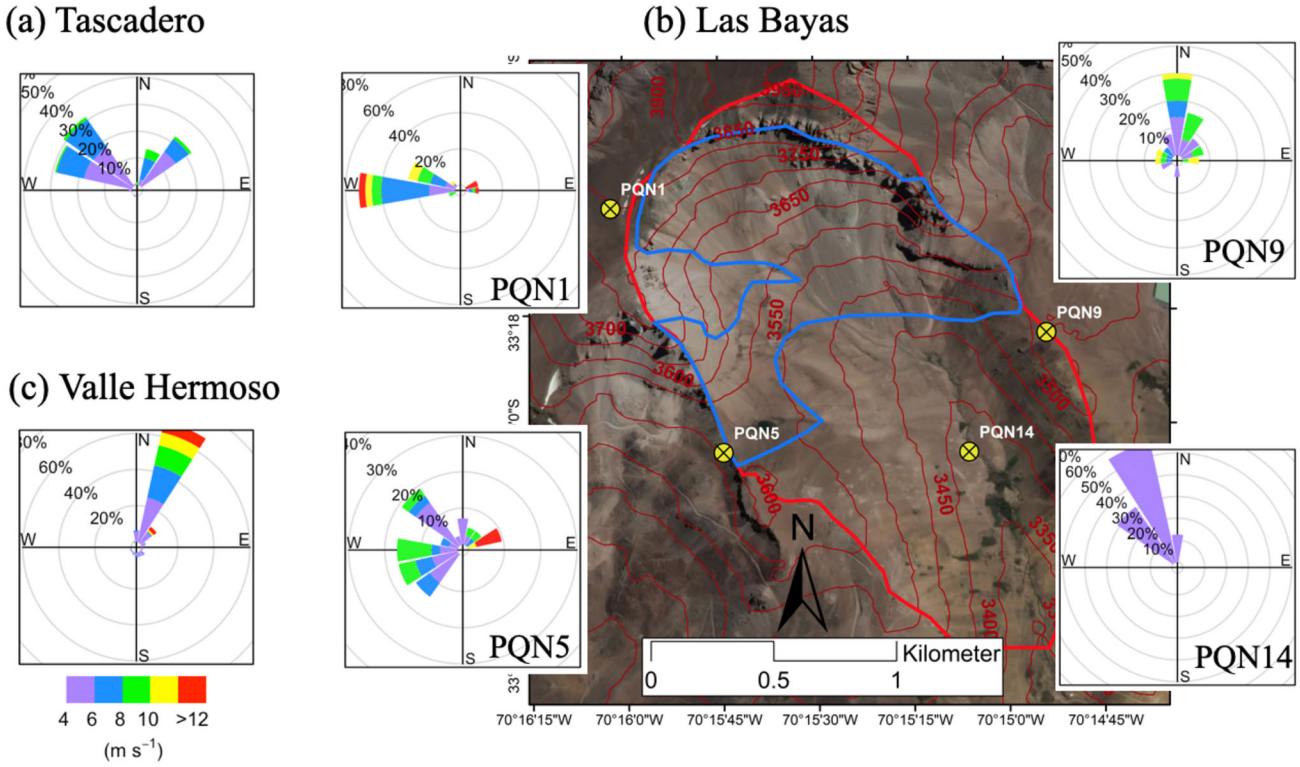

Figure 2. Wind roses for the 3 days preceding lidar scans, considering only wind speeds >4 m s^{-1}: (a) Tascadero (wind measured at Tascadero Station), (b) Las Bayas (wind measured at four different nodes, represented by yellow markers), and (c) Valle Hermoso (wind measured at Termas de Chillán station). The red line in the map is the watershed boundary, and the blue line is the TLS scan domain.

West, and VH East, respectively. Small negative DEM differences in the snow depth maps are set to zero when found to be consistent with snow cover area information derived from 3-m PlanetScope imagery (Planet Team, 2018), georeferenced to the lidar scan domain. Any negative differences that were identified as snow covered from the PlanetScope imagery were set to NoData. Following Kirchner et al. (2014), we ignored snow-covered pixels for slopes >55° to exclude well-known issues associated with vertical inaccuracies on high slope angles. This threshold was found to be consistent with the presence of snow in the PlanetScope imagery and the relationship of slope and snow depth presented by Shaw et al. (2020) in the same region. The slope and northness of the catchments were calculated from the snow-free DEM following Shaw et al. (2020).

3. Methods

3.1. Spatial Distribution

First, we conduct exploratory analyses to unravel possible links between snow depth and bare earth topography (the snow-free DEM), including slope and northness. In particular, we define 25-m elevation bands to compute average bare ground elevation and relevant snow depth statistics—including mean snow depth, standard deviation, coefficient of variation (CV) and skewness—to examine dependencies with elevation through correlation analysis. These snow depth descriptors are relevant for snow models that require prior knowledge of the statistical distribution that best represents the spatial variability within each model element (e.g., grid cells, subcatchments, elevation bands). Only nonzero snow depths are included (following López-Moreno et al., 2015; Skaugen & Weltzien, 2016; Winstral & Marks, 2014), and Spearman rank correlation coefficients with associated p values are computed to assess whether the relationships are statistically significant at the 95% confidence level. We also include the shape (α) and scale (β) parameters from the gamma distribution, which are derived from snow depth measurements within each band. The functional shape of the two-parameter gamma distribution (Wilks, 2011) follows the form:

$$f(SD) = \frac{(SD/\beta)^{\alpha-1}}{\beta\Gamma(\alpha)} \exp\left(-\frac{SD}{\beta}\right), \quad x, \alpha, \beta > 0 \tag{1}$$

where SD represents snow depth, and the parameters α and β can be estimated from the sample mean, and the standard deviation (Wilks, 2011):

$$\alpha = \frac{\overline{SD}^2}{s_{SD}^2} \tag{2}$$

$$\beta = \frac{s_{SD}^2}{\overline{SD}} \tag{3}$$

Finally, we compare the goodness of fit of three commonly used PDFs following Helbig et al. (2015) and Skaugen and Melvold (2019): normal, lognormal, and the two-parameter gamma functions (Equation 1). In this way, we assess the entire domain and each elevation band using the Anderson-Darling test (Delignette-Muller & Dutang, 2015), which equally assesses the main body of the distribution and the tails. If the p values are less than 0.05, we reject the null hypothesis that the snow depth measurements follow the tested distributions.

3.2. Variogram Analysis

The fractal concept has been used for decades to address problems in water resources science and engineering, operational hydrology being among the first fields that explored its potential (e.g., Hurst, 1951; Mandelbrot & Wallis, 1968). In principle, a fractal can be understood as an object whose subsets preserve the geometric or statistical characteristics of the whole undertransformations of scales (Mandelbrot, 1982)—a property referred to as *scale invariance* or *self-similarity*. To clearly distinguish from nonscaling sets, Mandelbrot (1982) proposed the compound term *scaling fractal*—also used as "fractal scaling" in snow hydrology (e.g., Deems et al., 2006; Mott et al., 2011; Veitinger et al., 2014) for the notion of a structure with infinite detail, and identical degree of irregularity across a range of temporal and/or spatial scales. Blöschl (1999) discussed ambiguities in the use of the term scaling, recognizing that it can be used for a broader sense of similarity and scale-invariance in the behavior of geophysical variables. Therefore, in this paper we do not use *scaling* (e.g., scaling regime, behavior, or pattern) and *fractal* indistinctly, recognizing that the latter implies detecting power laws and fractal dimensions (described below). The interpretation of a fractal pattern in a particular variable is that the same processes dominate within the range of temporal and/or spatial scales at which self-similarity is detected. Example applications have covered many hydrological variables (e.g., Alipour et al., 2016; Kirchner et al., 2000; Korres et al., 2015; Olsson et al., 1993), and in particular, snow depth (e.g., Clemenzi et al., 2018; Deems et al., 2006; Helfricht et al., 2014).

In this paper, we use variograms to examine the degree of spatial dependency in lidar-derived snow depths. Given a distance h, the semivariance can be computed as

$$\widehat{\gamma}(h) = \frac{1}{2|N(h)|} \sum_{(i,j) \in N(h)} \left(z_j - z_i\right)^2 \tag{4}$$

where z_i and z_j are snow depth values for points separated by a lag distance h, and $N(h)$ is the number of data points at the given lag distance h (Yates, 1948). If snow depth shows self-similar (i.e., fractal) behavior within a range of h, it should be possible to fit a power law with the form (Deems et al., 2006)

$$\gamma(h) = \alpha h^{\beta} \tag{5}$$

The exponent can be subsequently used to compute the fractal dimension, using the formula proposed by Mark and Aronson (1984):

$$D = 3 - \frac{\beta}{2} \tag{6}$$

The fractal dimension D can be understood as a measure of irregularity, or the capability of an object to "fill" the space in which it resides (Sun et al., 2006). Mathematically, it can be interpreted as an extension of the spatial dimensions of Euclidean geometry. Therefore, curves are characterized by fractal dimensions

between 1 and 2, while surfaces have associated D values between 2 and 3. In particular, $D \sim 2$ indicates a nearly planar Euclidean surface, while values close to 3 reflect more complex or "rougher" behavior.

Variograms are also used to detect possible anisotropies in snow depth scaling patterns. By definition, omnidirectional variograms include all snow depth point pairs regardless of their direction, whereas directional variograms include only point pairs within a specified direction. We binned the snow depth data before computing the variograms; in a trial and error procedure, we found that 46 bins distributed data in a sufficiently uniform manner when lag distance h was plotted on a log scale. At each site, we set the maximum lag distance to half of the maximum point pairs distance for variogram calculations (Sun et al., 2006) and define 16 angular classes of 22.5° for directional variograms. All variograms were computed using the "gstat" package (Pebesma, 2004), available in the statistical software "R" (http://www.r-project.org/). Snow depth scaling behavior is described as fractal within a specific distance range only if Equation 5 can be adjusted with $R^2 \geq 0.9$ (Deems et al., 2006, 2008; Mendoza, Musselman, et al., 2020) if this is the case, the associated fractal dimension is computed with Equation 6. The methodological steps used to detect scale break lengths are detailed in Appendix A. These analyses were first conducted for omnidirectional, and second for directional variograms to detect and characterize potential anisotropies in snow depth scaling patterns. It should be noted that this approach recognizes that a surface could be fractal within some range of lag distances and show no spatial correlation in others, a behavior that has been reported in the past for snow depth (e.g., Shook & Gray, 1996).

In this paper, we only report the adjustment of multisegment linear models in the log-log scale for experimental variogram points, though background analyses were performed to assess the quality of fit of alternative models from the geostatistical palette, including exponential, Gaussian, and spherical, following Mendoza, Musselman, et al. (2020). The results demonstrate that the multisegment log-log linear models outperform the alternatives when adjusted for the entire distance range in terms of correlation, biases, and root-mean-square errors (see Figures S2–S5 in the supporting information). Additionally, comparable results with log-log linear models can be obtained for specific combinations of domains and distance ranges if the alternative models are adjusted for each scaling range separately (not shown).

To examine possible factors explaining snow depth scaling patterns and detected anisotropies, we also compute and analyze omnidirectional and directional variograms for the bare earth topography. Finally, we use the term "multiscale behavior" when two or more fractal patterns separated by scale breaks are found (as Clemenzi et al., 2018), instead of the term "multifractal" (Deems et al., 2006; Schirmer & Lehning, 2011), since the latter is typically considered to involve a continuous spectrum of fractal dimensions (Mandelbrot, 1988).

3.3. Transect Analysis

Shook and Gray (1996) hypothesized (later confirmed by Trujillo et al., 2007 for a suite of sites in Colorado, USA) that the scale length of snowdrifts (the distance between drift or dune peaks) is related to snow depth scale breaks (identified from variogram analysis) in wind-prone areas. We assess this (following Trujillo et al., 2007) through the examination of snow depth transects across four directions (S-N, W-E, NW-SE, SW-NE), with the aim to unravel possible connections between scale break lengths, wind direction, and the distance between local maxima snow depth values. First, we define up to three equidistant profiles or transects for each lidar data set and direction (see Figure S6 in the supporting information). Second, we seek local maxima snow depths at each transect by identifying at least m consecutive positive (or negative) changes. After an iterative process that involved visual inspection, we set $m = 3$ and define a threshold equal to the first tercile of nonzero snow depth measurements to disregard small local maxima points that could result from slight variations along the profiles analyzed. Once the local maxima snow depth points were identified, we compute the separation distance d between peaks and derive the empirical distributions of d by grouping all transects for a specific direction.

4. Results

4.1. Snow Depth Distribution

Figure 3 displays lidar-derived snow depth maps (Column 1), and spatial distributions (presented as boxplots) per 25-m elevation bands (Column 2), 5° slope intervals (Column 3), and 10° northness bins

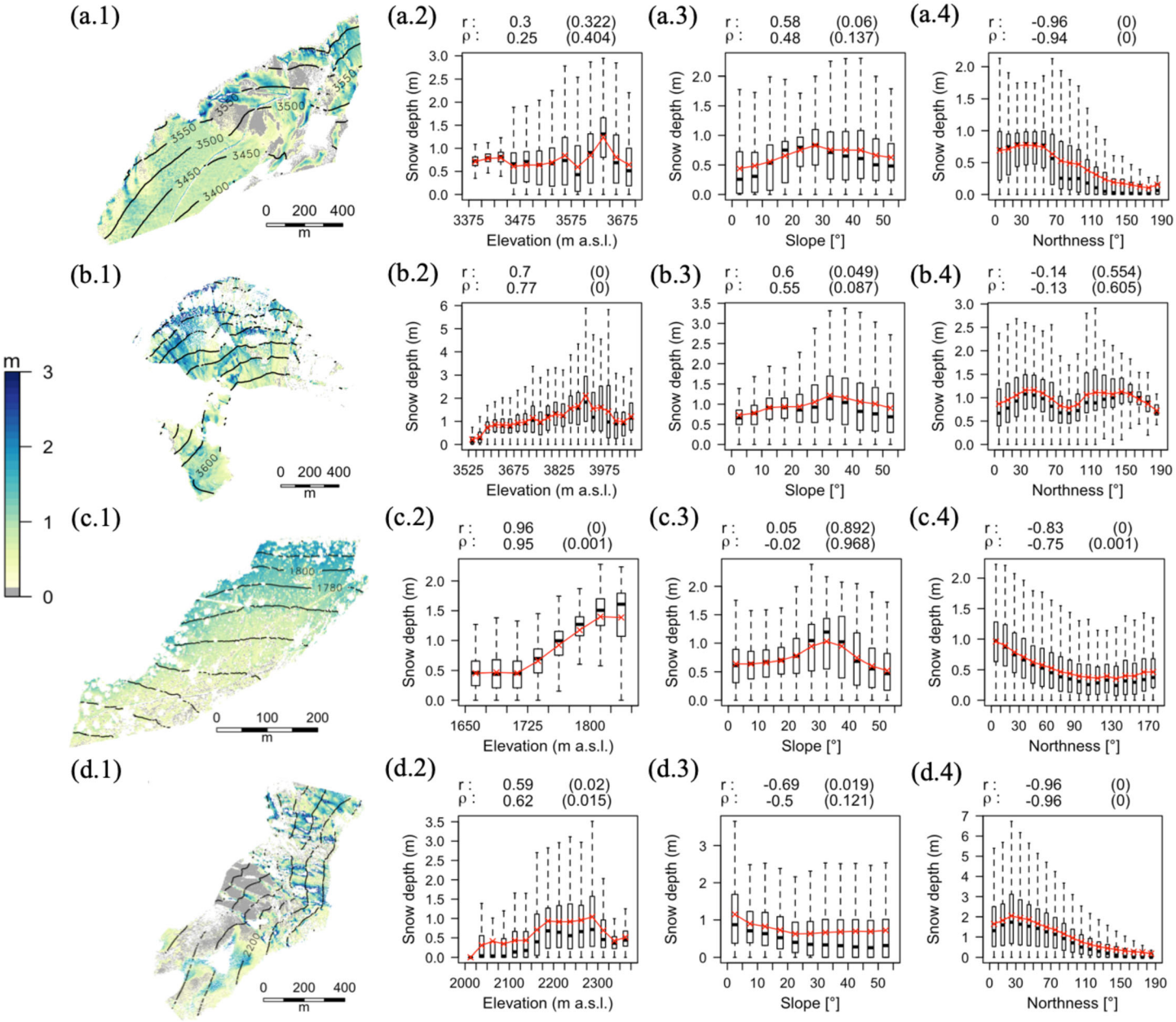

Figure 3. Lidar-derived snow depth maps (column 1) and snow depth distributions per 25-m elevation bands (column 2), 5° slope intervals (column 3), and 10° northness bins (column 4) for all study sites: (a) Tascadero, (b) Las Bayas, (c) Valle Hermoso West, and (d) Valle Hermoso East. In the left panels, snow depth values >3 m (i.e., 0.2% in Tascadero, 1.4% in Las Bayas, 0% in VH West, and 2.5% in VH East) have been masked out for visualization purposes, and zero snow depths are shown in gray. In columns 2–4, outliers have been discarded, zero snow depths are included, the red crosses represent mean depths across bins, and the strength of the relationship between those means and bin-averaged topographic predictors is quantified by correlation coefficients (Pearson correlation r and Spearman rank correlation ρ) and p values (in parenthesis). For northness, 0° indicates south facing, while 180° indicates north-facing locations.

(Column 4). Possible relationships between band-averaged snow depths and topographic variables are examined using Pearson (r) and Spearman's rank (ρ) correlation coefficients. No altitudinal gradients are observed in Tascadero, whereas strong correlations with altitude are found at Las Bayas and VH West. Additionally, all nonvegetated areas show decreasing snow depths with higher elevation, starting from a site-specific altitude threshold. In Las Bayas, these higher elevation sites coincide with steep cliffs that surround the cirque of the catchment. In VH East, the highest areas are exposed to strong winds and solar radiation, given their orientation to the north and relative position to the ridge that delineates the catchment boundary. Correlations with slope are found in all sites except VH West, and significant

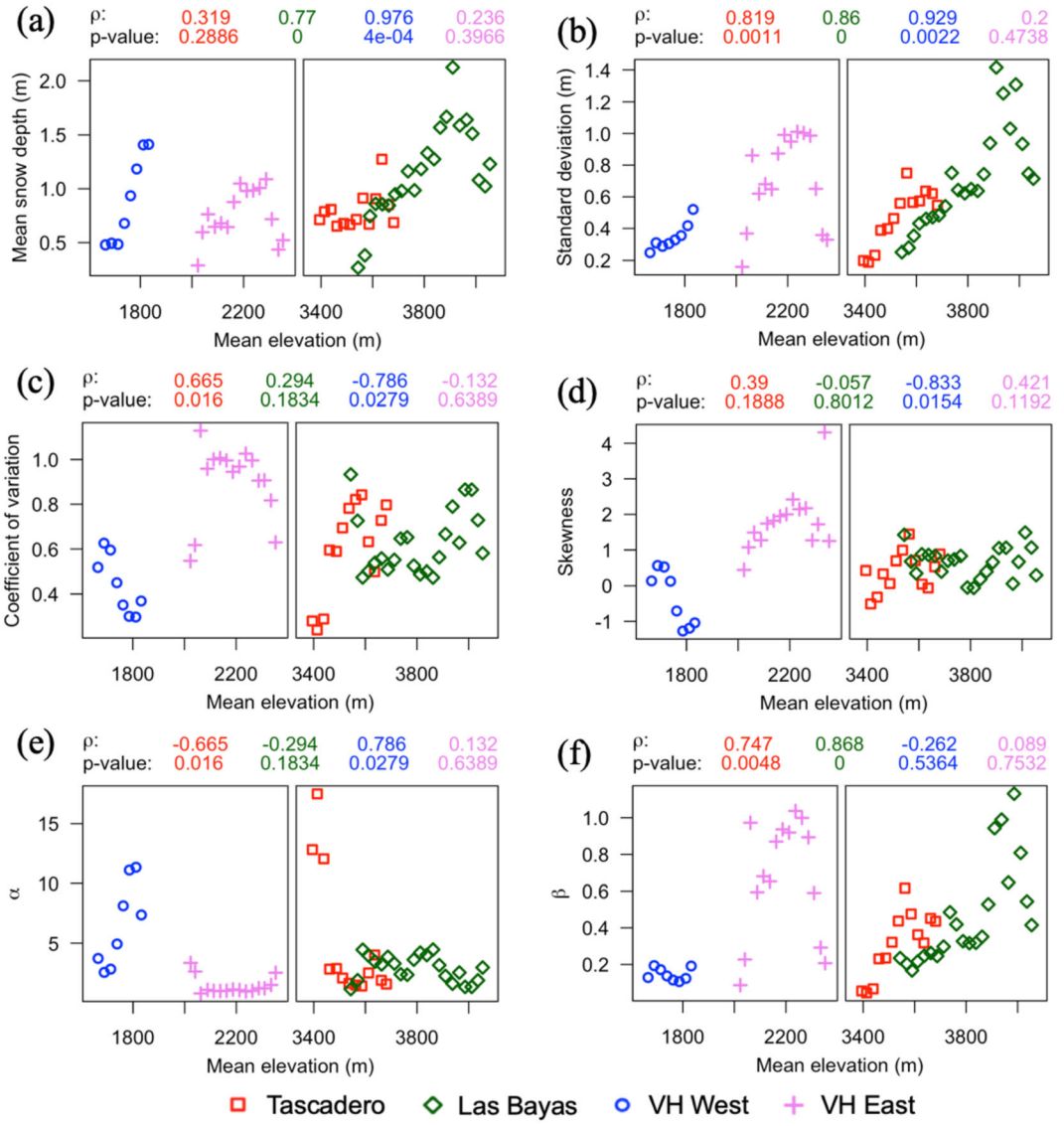

Figure 4. Snow depth statistics as a function of mean elevation at 25-m elevation bands: (a) mean snow depth, (b) standard deviation, (c) coefficient of variation, (d) skewness, (e) α and (f) β parameters from the gamma distribution. Only nonzero snow depth values are included and the strength of the relationship is quantified by Spearman rank correlation coefficients (ρ) and p values.

relationships with northness are observed in all subdomains excepting Las Bayas. We also fitted a Gaussian Kernel smoother for snow depth as a function of elevation, and computed correlations between detrended snow depths (using the Kernel estimates) and slope/northness, finding similar dependencies (not shown).

Possible relationships between snow depth statistics and average elevation are further examined in Figure 4, which includes only nonzero depths. Statistically significant ($p < 0.05$) correlations between mean terrain elevation and mean snow depth are obtained in Las Bayas and VH West (Figure 4a), and positive ($\rho > 0.80$) correlations with standard deviations are observed in Tascadero, Las Bayas, and VH West (Figure 4b). Both CV (Figure 4c) and skewness (Figure 4d) significantly decrease with elevation in the latter site, and CV shows significant, positive trends in Tascadero. Additionally, snow depth is positively skewed in most elevation bands across nonvegetated sites and shows a relatively steadier behavior with elevation in Las Bayas. Mixed altitudinal trends are obtained for the shape parameter α, with significant correlations only at Tascadero ($\rho \sim -0.67$) and VH West ($\rho \sim 0.79$), while both semiarid locations (Tascadero and Las Bayas) provide $\rho > 0.75$ for the scale parameter β. At VH East, a step behavior can be seen around 2,150, m a.s.l.: below

this elevation, a significant fraction of the slope is oriented more to the north, and increased radiation loads explain the lower snow depths observed in those sites (even with many pixels showing no snow cover). Such an elevation threshold coincides with a transition to steeper slopes in bare earth topography. Possible dependencies between snow depth statistics and band-averaged snow depth were also explored, finding that the standard deviation is positively correlated with mean snow depth in all scanning areas (with $\rho > 0.89$ in Las Bayas and Valle Hermoso), and significant (negative) correlations between CV/skewness and mean snow depth only in VH West (see Figure S7 in the supporting information).

Figure 5 illustrates the goodness of fit of alternative parametric distributions for snow depth through the Anderson-Darling (A-D) and Kolmogorov–Smirnov ($D_{K\text{-}S}$) statistics, and associated p values. Lower A-D or $D_{K\text{-}S}$ values indicate better fits, and the results are displayed for the full domains (left panels, a–d)—each at 1-m horizontal resolution—and 25-m elevation bands (right panels, e–g). When examining full domains (Figures 5a–5d), it is observed that all goodness-of-fit evaluations reject the null hypothesis that the sampled depths follow the tested distributions ($p < 0.05$). In Las Bayas and VH East, the gamma distribution provides the best compromise between graphical adjustments and A-D or $D_{K\text{-}S}$ scores. Although the lowest A-D and $D_{K\text{-}S}$ statistics in the remaining sites are obtained through normal distributions, good adjustments to snow depths are difficult to obtain—especially in Tascadero, where a bimodal distribution is observed. The A-D results obtained for individual elevation bands (Figures 5e–5g) show that normal distributions are generally the ones with the best fit in Tascadero and VH West, while gamma distributions have the lowest A-D scores in VH East. Mixed results are obtained in Las Bayas, where the lowest A-D statistics alternate between normal and gamma fits, and the largest A-D scores are obtained with lognormal distributions in most elevation bands. Anderson-Darling tests reject, in most elevation bands, the null hypothesis that the sample snow depths followed normal, lognormal, or gamma distributions. Similar relative performances are obtained from the application of Kolmogorov-Smirnov tests across elevation bands (see Figure S8 in the supporting information).

4.2. Scaling Patterns

The analysis of omnidirectional snow depth variograms (Figure 6a) reveals the existence of primary (L_1) and secondary (L_2) scale break lengths in all sites, defining regions with different spatial structures. In unvegetated areas, primary scale break lengths span 15–21 m (Table 3). Moreover, a secondary scale break is detected across all scanning areas, with L_2 in the 67–188 m range in nonvegetated areas. In VH West, shorter scale break lengths ($L_1 \sim 4$ and $L_2 \sim 39$m) are detected. Such scanning area corresponds to a forest clearing originated by past burnings, and the terrain is scattered with shrubs, smaller new trees, and fallen tree trunks and logs.

Interestingly, multiscale behavior in snow depth is detected in all sites (Figure 6a), so we make the distinction between short-range (D_S), medium-range (D_M), and long-range (D_L) fractal dimensions (Table 3). In nonvegetated areas, very similar fractal dimensions D_S (~2.5) and D_M (~2.9) are obtained, while larger values ($D_S \sim 2.64$ and $D_M \sim 2.94$) are observed in VH West. A long-range fractal dimension region is detected in Las Bayas and VH West, with D_L values equal to 2.83 and 2.76, respectively. To unravel possible links between snow depth and bare earth topography structures, we analyze omnidirectional variograms for the latter variable (Figure 6b), finding very similar fractal dimensions across sites. It should be noted that, although scale breaks are detected in Tascadero and VH East, no fractal behavior is found beyond those break lengths.

Figure 7 displays radar plots for scaling properties, including the fractal dimension for bare earth topography (D), short-range fractal dimension for snow depth (D_S), and the primary scale break length for the same variable. At all sites, the smallest D values for bare earth topography (Figure 7a) are found to be parallel to the general terrain orientation (see left panels in Figure 3), and smoother anisotropies are found in the semiarid subdomains (i.e., Tascadero and Las Bayas). Figure 7b shows that the directionality of anisotropies in D_S vary among sites: while negligible variations are observed in Tascadero, the largest values in VH East are aligned with dominant local winds (Figure 2). In Las Bayas, the largest D_S values are perpendicular to the large-scale terrain trend (SW–NE) with local maxima at many directions, suggesting a joint effect of local winds and topography. For VH West, directional D_S range 2.65–2.85, with slightly larger values aligned with locally measured winds. Regarding scale break anisotropies (Figure 7c), different patterns are observed across sites:

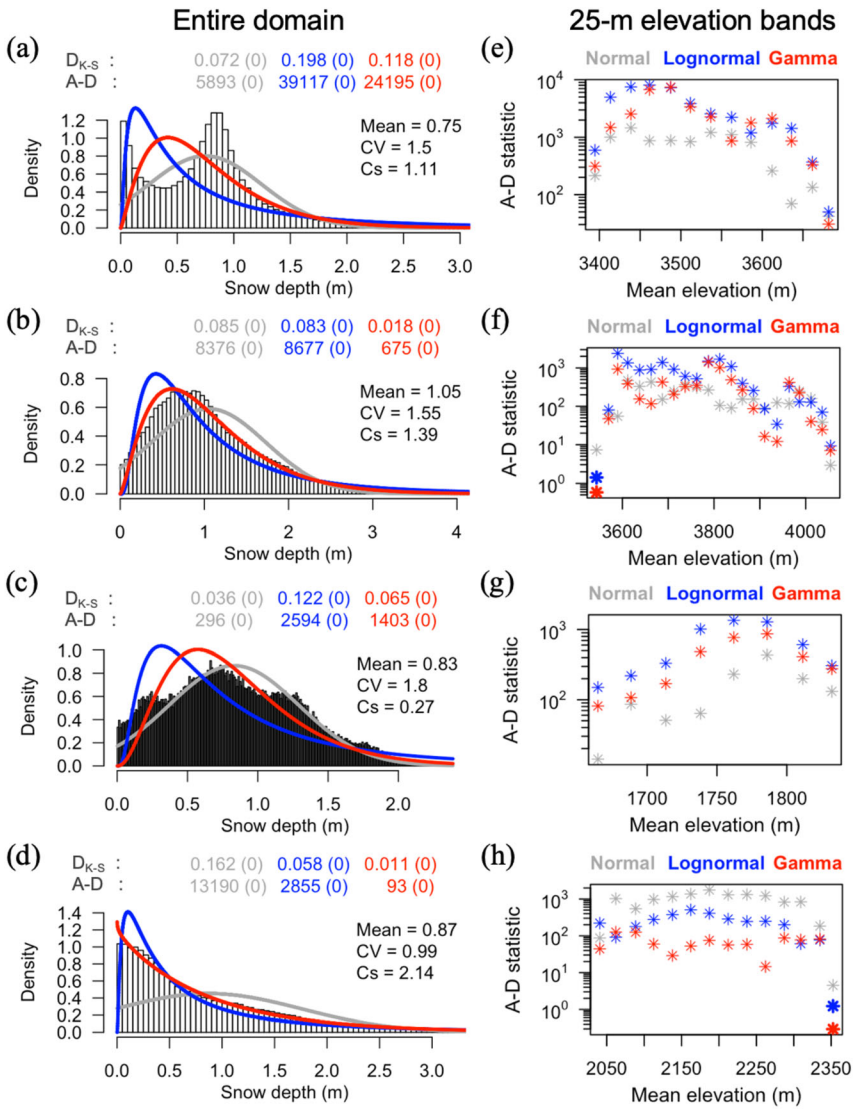

Figure 5. (left) Empirical distribution of snow depth from lidar measurements and fitted theoretical normal, lognormal, and gamma distributions for the entire domains: (a) Tascadero, (b) Las Bayas, (c) Valle Hermoso West, and (d) Valle Hermoso East. CV and Cs denote coefficient of variation and skewness, respectively. Anderson-Darling (A-D) and Kolmogorov–Smirnov ($D_{K\text{-}S}$) statistics are displayed for each distribution, and associated p values are included between parentheses. (right) A-D statistics for each 25-m elevation band and site (e–h panels), where bold symbols indicate that the null hypothesis (i.e., that snow depth measurements follow the colored distribution) is accepted at a 5% significance level. In all panels, density distributions and goodness-of-fit statistics are color coded as gray (Normal), blue (Lognormal), and red (Gamma).

larger L_1 values are aligned perpendicular to dominant winds in Tascadero, Las Bayas and VH East (alpine sites with differing climates), while no clear connections with wind are observed in VH West.

In summary, dominant wind direction, anisotropies in bare earth topography (i.e., terrain orientation) and L_1 seem to be somehow connected in Tascadero, but no direct links with D_S are observed. In Las Bayas, anisotropies in terrain D and snow depth D_S are nearly parallel, while the largest values in L_1 (N-S) are perpendicular to preceding westerly winds. In VH East, preceding wind is parallel to the largest values in fractal dimensions D and D_S, and nearly perpendicular to L_1 anisotropy. Finally, no apparent connections between topography, wind, and snow depth scaling properties are found in VH West, which might be due to specific terrain characteristics, topographic sheltering, and, importantly, the presence of vegetation.

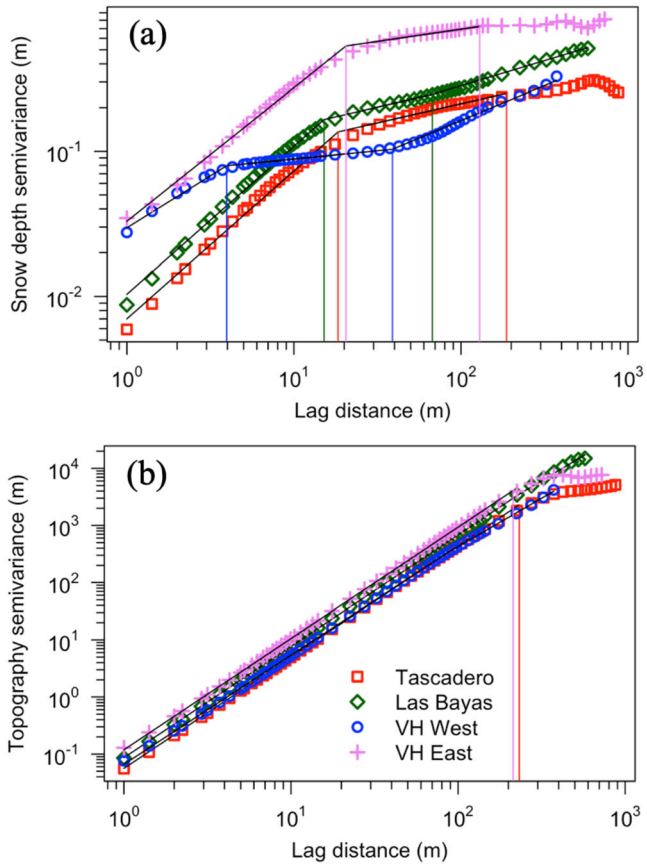

Figure 6. Omnidirectional variograms for (a) snow depth and (b) bare earth topography in all study sites. Vertical lines represent scale break lengths, and diagonal black lines represent log-log linear models with $R^2 \geq 0.9$.

4.3. Snow Depth Profiles

Our results suggest that landscape properties, and in particular vegetation cover, are key controls on the spatial structure of snow depth along the extratropical Andes. This idea is examined with sample profiles of snow depth along the NW-SE direction for all study sites (Figure 8). One can note the general tendency of increasing snow depths with elevation in Las Bayas and VH West, as shown in Figures 3 and 4a. The transects in VH West (Figure 8c) indicate that high-frequency variations (i.e., short wavelengths) dominate snow depths in this area. Such behavior is also observed for other transects delineated in the same or different directions (see Figure S9 in the supporting information). Conversely, low-frequency variations dominate along snow depth transects in our alpine, unvegetated sites (Figures 8a, 8b, and 8d). The contrasting shapes of snow depth profiles at VH West and VH East show the large effects of scattered vegetation on snow scaling patterns, in particular on the shorter scale breaks obtained in the former site.

A natural question from here is to what extent scale break magnitudes are related to the separation distance d between local peaks (red circles in Figure 8) To answer this, we examine the empirical distribution functions of this variable across four directions in all sites, and compare the sample means between distributions (Figure 9). As expected, the average d values in the shrub-dominated VH West (8.6–13 m) are smaller than those obtained for all unvegetated sites, which fluctuate between 13 and 21 m —that is, the same order of magnitude as L_1 (Table 3; Figures 6a and 7c). Furthermore, the largest average d values at Tascadero and Las Bayas are obtained along SW-NE and S-N directions, respectively, in agreement with anisotropies observed in L_1 (Figure 7c). Such correspondence between directional d and L_1 magnitudes is not, however, observed at Valle Hermoso.

5. Discussion

5.1. Topographic Controls and Statistical Distribution

Exploratory analyses on the relationship between snow depth and bare earth topography reveal an increase up to a certain elevation. This behavior has been reported, for example, for lidar-derived snow depths in the southern Sierra Nevada (Kirchner et al., 2014; Zheng et al., 2016), and also across sites within the European Alps and the Spanish Pyrenees, at both hillslope and subcatchment (1–5 km^2) scales (Grünewald et al., 2014). The decline in snow depth at very high elevations has generally been explained by the heightened interaction of snowfall, terrain, and wind redistribution, with Grünewald et al. (2014) explaining the snow depth inflection point as that occurring at the transition between gentler, soil-covered slopes, and steeper alpine rock. The specific nature

Table 3
Omnidirectional Fractal Parameters (D_S, D_M, D_L, L_1, and L_2) for the Observed TLS Snow Depth Distributions

	Short-range		Medium range		Long range		L_1	L_2
Site	R^2	D_S	R^2	D_M	R^2	D_L	m	m
Tascadero	0.99	2.49 (2.47–2.52)	0.96	2.87 (2.86–2.88)	0.21	—	18.4	187.6
Las Bayas	0.99	2.49 (2.47–2.51)	0.99	2.87 (2.86–2.87)	0.99	2.83 (2.82–2.84)	15.2	67.4
VH West	0.97	2.64 (2.59–2.7)	0.99	2.94 (2.94–2.94)	0.98	2.76 (2.75–2.77)	4.0	38.9
VH East	0.99	2.54 (2.52–2.55)	0.95	2.92 (2.91–2.92)	−0.02	—	20.5	129.5

Note. For fractal dimensions, 95% confidence intervals are displayed in parenthesis.

Table 4
Omnidirectional Fractal Parameters (D and L_1) for the Observed TLS Bare Earth Elevation Distributions

Site	Log–log linear model		L
	R^2	D	m
Tascadero	0.99	2.03 (2.02–2.03)	232.4
Las Bayas	0.99	2.03 (2.02–2.03)	—
VH West	0.96	2.04 (2.04–2.05)	—
VH East	0.99	2.03 (2.02–2.03)	213.6

Note. For fractal dimensions, 95% confidence intervals are displayed in parenthesis.

of the depth-elevation relationship is also influenced by the scale at which measurements are obtained. In our study sites, elevation ranges are in the order of 200–500 m. Ayala et al. (2014) explored a data set of manually collected snow depth observations in different hillslopes spanning an elevation range of 1,200 m, finding a stronger dependency, coherent with documented orographic enhancement of precipitation.

Possible dependencies between band-averaged elevation and snow cover variability metrics (i.e., standard deviation, coefficient of variation, and skewness) vary considerably across sites, which is expected due to discrepancies in vegetation cover, elevation range, and wind exposure (e.g., Grünewald et al., 2014; Zheng et al., 2016). In agreement with Skaugen and Melvold (2019), we found significant positive correlations between band-averaged snow depth and standard deviation (Figure S7a), but weak relationships with CV and skewness in alpine, unvegetated sites. These results are still encouraging, since the standard deviation of snow depth depends on a dynamic parameter (i.e., mean snow depth), and a static parameter (band-averaged terrain elevation, Figure 5b) in alpine sites. Therefore, the simple nonlinear relationship proposed by Skaugen and Weltzien (2016) could be used to simulate and predict the snow depth variance as a function of the mean in any type of hydrologic response unit along the extratropical Andes. Although we only examined possible dependencies using elevation bands and average terrain elevations, any other topographic variables, in addition to land cover type, could be used to stratify model parameters (e.g., Skaugen & Melvold, 2019).

The comparison between full-domain snow depth statistics (Figure 5) and those obtained for individual elevation bands (Figure 4) simply confirm earlier findings on the limited transferability of distribution functions and related parameters to smaller subdomains (e.g., Marchand & Killingtveit, 2005). We found that the lognormal distribution was generally outperformed by the normal or the two-parameter gamma distributions across 25-m elevation bands and that the latter distribution outperforms the lognormal distribution when assessing goodness of fit for full domains. A similar relative performance was obtained by Winstral and Marks (2014) for the Reynolds Mountain East catchment (0.36 km^2); by Helbig et al. (2015) for spatial scales <500 m in eastern Switzerland and the eastern Spanish Pyrenees; and by Skaugen and Melvold (2019), who concluded that the gamma distribution was the most suitable for the majority (68%) of the 500 m × 1 km (0.5 km^2) grid cells analyzed across Hardangervidda in Southern Norway.

5.2. How Does Snow Depth Scaling in the Andes Compare to Other Mountain Regions?

The multiscale behavior of snow depth in our Andean sites is somewhat consistent with previous findings in the Colorado Rocky Mountains (Deems et al., 2006, 2008; Trujillo et al., 2007, 2009), the Swiss Alps (Clemenzi et al., 2018; Mott et al., 2011; Schirmer & Lehning, 2011), and the Ötztal Alps, Austria (Helfricht et al., 2014),

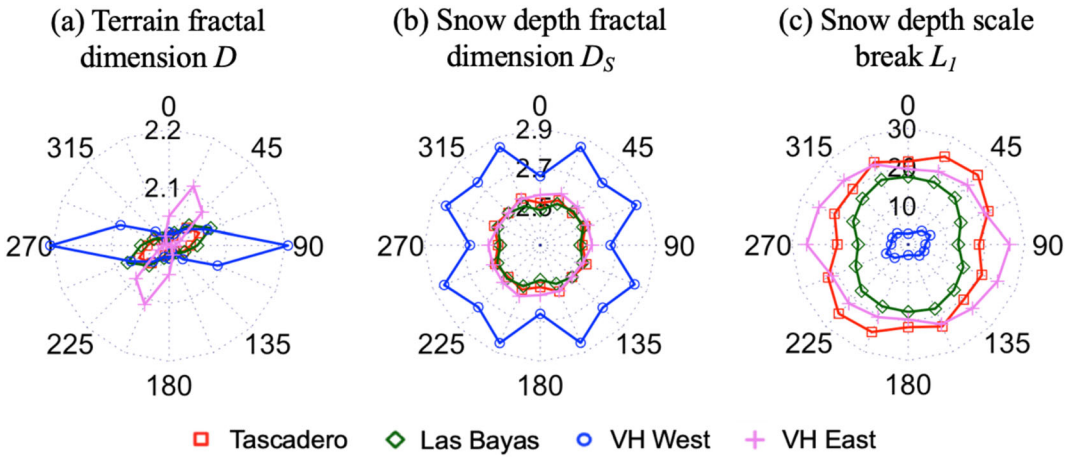

Figure 7. Fractal parameters by azimuth: (a) fractal dimension for bare earth topography, (b) short-range fractal dimension, and (c) primary snow depth scale break (m).

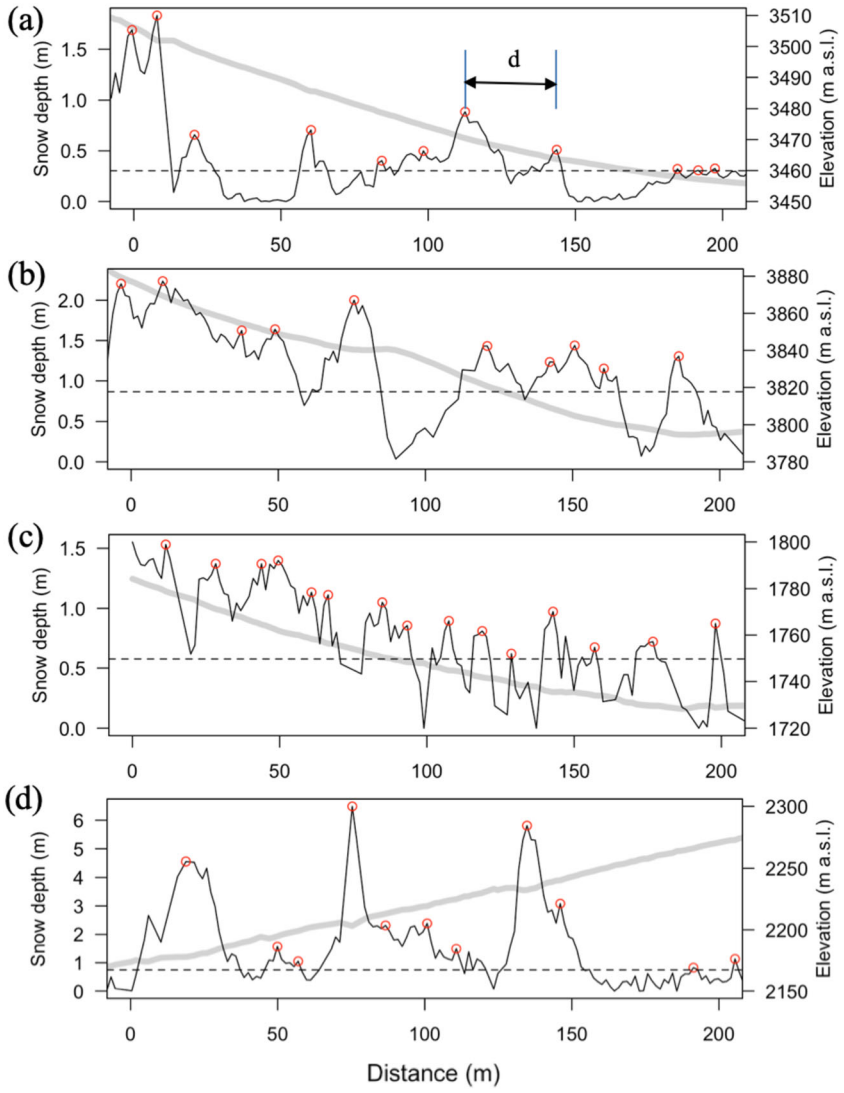

Figure 8. Sample snow depth profiles (thin black lines) and bare earth topography profiles (gray thick lines) along the NW-SE orientation for all domains: (a) Tascadero, (b) Las Bayas, (c) Valle Hermoso West, and (d) Valle Hermoso East. Transects have been truncated up to a maximum distance of 200 m for comparison purposes. The red points indicate the location of all local peaks above a threshold (dotted line) equal to the first tercile of nonzero snow depth measurements, and the variable "d" denotes the distance between these peaks.

where two fractal regimes were obtained, separated by scale break distances that varied depending on site characteristics (e.g., land cover, exposure to wind). For instance, Trujillo et al. (2009) reported discrepancies in the snow depth scaling behavior of two areas with similar topography, but different wind influences and vegetation, finding scale breaks approximately 6 times larger in a tundra subdomain compared to a forested area. Schirmer and Lehning (2011) obtained different scale breaks in wind-protected (6 m) versus wind-exposed (20 m) slopes in an alpine, nonvegetated domain. In this study, we found larger D_S and smaller L_1 (~4 m) values in the shrub-dominated VH West compared to the alpine, nonvegetated subdomains (L_1–15–21 m for omnidirectional variograms). Because the latter sites encompass very different hydroclimatic conditions (Table 2), we suggest that local topography and vegetation cover are dominant controls for snow depth spatial structure, rather than climatological characteristics (e.g., aridity index, mean winter precipitation). Moreover, the primary scale breaks for our alpine sites align well with those found in other ice-free areas near maximum accumulation dates (Helfricht et al., 2014; Mendoza, Musselman, et al., 2020; Mott et al., 2011; Schirmer & Lehning, 2011), although our short-range fractal dimensions seem slightly larger in comparison to the regions examined therein.

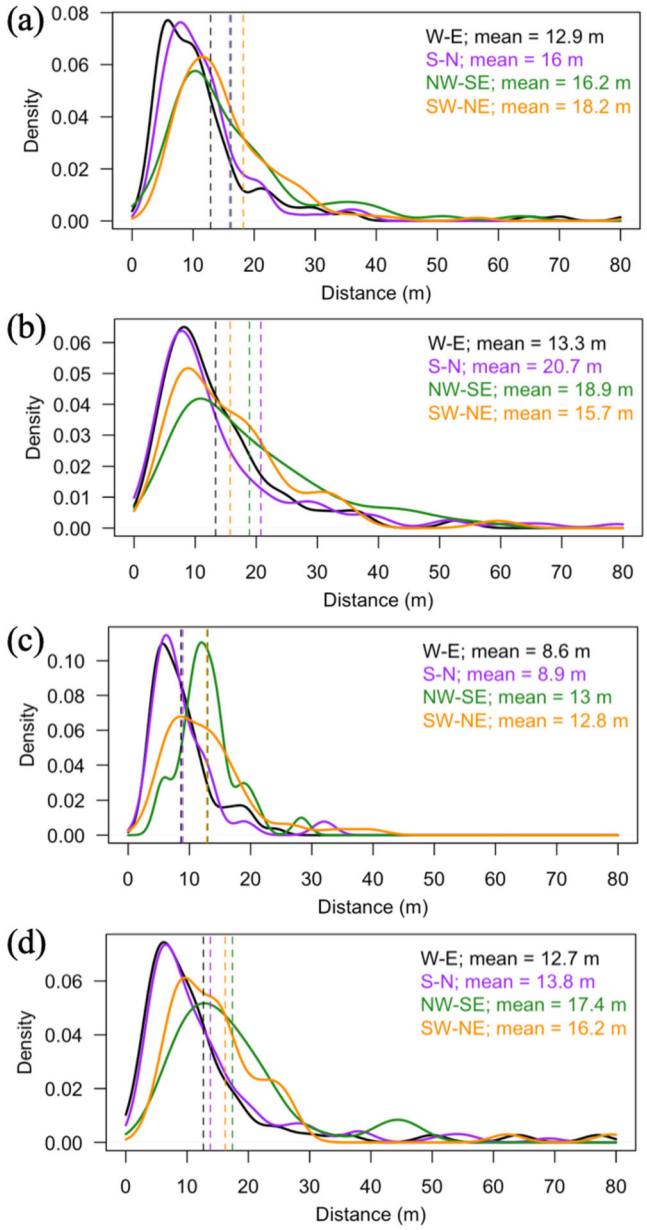

Figure 9. Empirical distribution functions of the separation distance "d" between peaks in the snow depth profiles. Each curve compiles d values obtained from two or three directional transects within the analyzed domain, and dashed vertical lines indicate the location of sample means. The results are displayed for (a) Tascadero, (b) Las Bayas, (c) Valle Hermoso West, and (d) Valle Hermoso East.

The secondary scale break lengths detected here span 38–190 m, which are smaller than those reported by Mendoza, Musselman, et al. (2020) for the Izas experimental catchment (>200 m in multiple lidar scans). Nevertheless, our results differ from previous studies in that we obtained up to three fractal regimes in two sites (Las Bayas and VH West), a behavior previously unreported and somewhat unexpected considering the absence of multiscale behavior in bare earth topography (Figure 6b). We speculate that the scattered distribution of shrubs plays a key role in VH West—where the change in scaling patterns is better defined (see Figure 6a and Table 3) –, although this cannot be confirmed due to the lack of lidar-derived maps for topography and shrub height. Shrub structure on sloped terrain is difficult to resolve with airborne lidar (Glenn et al., 2011) and the challenges are compounded for TLS (Currier et al., 2019). For Las Bayas, the small difference between D_M and D_L suggests that some process interactions are simply enhanced beyond the secondary scale breaks, producing slope changes larger than 20% in variograms at the log-log scale.

The terrain scaling anisotropies reported here agree with previous findings of Deems et al. (2006) and Mendoza, Musselman, et al. (2020), who obtained smaller bare earth fractal dimensions parallel to terrain orientation in the Colorado Rockies and the Spanish Pyrenees, respectively. Nevertheless, these anisotropies, prevailing wind directions and snow depth fractal parameters relate differently depending on the subdomain analyzed, or simply do not relate at all (like in VH West), which is not surprising if one explores past studies. For example, Deems et al. (2006) and Schirmer and Lehning (2011) obtained the largest D_S values perpendicular to prevailing winds, Clemenzi et al. (2018) found these to be parallel to prevailing winds, while Mendoza, Musselman, et al. (2020) found negligible directional variations in this parameter.

Regarding scale break anisotropies, we found the largest L_1 values nearly perpendicular to dominant, preceding winds in the three alpine sites—in agreement with Schirmer and Lehning (2011)—regardless of the large differences in hydroclimatic characteristics (Table 2). The same anisotropies were observed at Tascadero and Las Bayas (semiarid, alpine environments) for the mean horizontal distance between local peaks (d) in the snow depth surface. Possible connections between the above anisotropies, dominant winds, and directional variations in second scale breaks (L_2) are more difficult to establish, since the latter were not detected for all azimuth angles in our alpine sites (not shown). Indeed, directional L_2 in Tascadero (with prevailing northwesterly winds) and VH East (with prevailing northern winds) was only found along 67.5° (160 m) and 0° (222 m), respectively. In Las Bayas (where preceding winds were westerly), the longest L_2 value (375 m) was obtained for 22.5°, whereas anisotropies in L_1 and L_2 were found to be very similar in VH West. Mendoza, Musselman, et al. (2020) also found that L_2 may not be a temporally consistent property of snow depth distribution—unlike D_S and L_1. Therefore, these secondary scale breaks—either omnidirectional or directional—should be interpreted with caution, since their existence may result from complex interactions between local meteorology, topography, and land cover properties.

The results from transect analyses across all Andean sites confirm that the primary scale break L_1 is a measure of the average distance d between local peaks in snow depth, as reported by Trujillo et al. (2007) for the Colorado Rocky Mountains, following earlier suggestions that the formation of snow drifts define subdomains of high spatial autocorrelation (Shook & Gray, 1996). Past studies have attributed the existence and location of local snow depth peaks to interactions between wind, snow, and land characteristics—e.g.,

terrain exposure, local irregularities, vegetation (when present)—whose relative importance varies depending on local site conditions (e.g., Schirmer & Lehning, 2011; Trujillo et al., 2007, 2009). In this study, the similarity between L_1 and d values (13–21 m) in alpine Andean sites and anisotropies related to wind directions indicate that snowdrift formation is strongly related to wind-coupled processes, in agreement with the results obtained by Schirmer and Lehning (2011) and Mott et al. (2011) for wind-exposed and wind-protected subareas. On the other hand, the lack of clear relationships between anisotropies in fractal parameters and preceding winds in VH West suggests that interception could be a key control of snow depth variability in this subdomain, although better wind measurements are required to support this hypothesis.

5.3. Implications for Snow Modeling

Overall, the exploratory analyses and goodness-of-fit tests have practical implications for distributed snow modeling in the extratropical Andes Cordillera. The results from our variogram analyses provide detailed information on distance ranges where scale-invariance is observed, guiding the selection of model scales in high-resolution distributed snowmelt models (e.g., Clemenzi et al., 2018; Trujillo et al., 2007). Trujillo et al. (2007) suggested that short-scale variations in snow depth are driven by local processes such as canopy interception and the interaction between winds and topographic irregularities (e.g., concavities, rocks), while longer-range snow patterns can be attributed to the average effects of redistribution by wind and canopy effects (when present). If the primary goal is to provide a detailed snow process estimation, the minimum model scale that our data suggest is 1 m (i.e., the lidar-derived data resolution), while the recommended maximum model scale will depend on directional and omnidirectional L_1 values: 2.5 m in VH West, and 12 m for Las Bayas, and 18 m for the remaining sites. These model resolutions are coherent with the scales of drift formation, which has been suggested to control the timing of melt and runoff generation in alpine basins, particularly late in the melt season when persistent drifts can serve as local ecological refugia (e.g., Marshall et al., 2019). Thus, appropriate modeling of snow drift magnitude and location may be desirable for model applications where localized snow persistence has the potential to impact basin-aggregated estimates of summer low-flow conditions, water limitation, and vegetation productivity. This topic is particularly relevant for future climate impact projections (Xu et al., 2019). The fact that the shortest scale break length (2.5 m) happens at the VH West site, where modest shrubs are present, suggests that detailed representations of mass and energy fluxes between snow and vegetation are required to adequately simulate snow depth variability. This is in agreement with the findings of Broxton et al. (2015) and Harpold et al. (2020), although additional data are required to explore the effects of deciduous trees typical of southern South America on snow dynamics.

Modeling efforts oriented toward water resource applications require snow simulations at the watershed or larger scales. In such cases, subelement variability should be addressed regardless of the modeling units used (e.g., grid cells, elevation bands, hydrologic response units) and depletion curves, which relate the coevolution of snow-covered area and snow water equivalent, provide an opportunity for incorporating this variability in a parsimonious manner (Liston, 1999; Luce & Tarboton, 2004). Snow depletion curves can be derived from theoretical PDFs, or from SWE or snow depth observations when available. Our results show that, although theoretical PDFs could approximate the snow depth data obtained at each site, there are considerable variations in the shape of the distribution at the hillslope scale, so that the subjective choice of the lognormal distribution in subgrid parameterizations (e.g., Cortés et al., 2016; Cortés & Margulis, 2017) should be revised whenever data are available. It must be remembered, however, that subgrid parameterizations can be more sensitive to distribution parameters than to the functional form selected (Luce & Tarboton, 2004) and that such parameters are highly variable in space (e.g., López-Moreno et al., 2015).

The results presented in this paper show that elevation and associated effects of orographic precipitation enhancement play a limited role in the spatial variability of snow depth across the subdomains examined. Conversely, northness and slope strongly influence this variable, suggesting that a regional scale modeling effort should explicitly account for orographic precipitation enhancement at a horizontal resolution that can resolve this process (e.g., see Ayala et al., 2014), while representing hillslope scale variability presented here. Since the elevation range spanned by our lidar-derived data sets fluctuates between 300 and 500 m, a HRU-based discretization with elevations spanning those intervals could be a reasonable first approximation. Within these larger subregions, variability could be represented using snow depletion curves or interconnected representative hillslopes (Swenson et al., 2019). In forested regions, further work is needed

to properly quantify the effect of vegetation on the snowpack energy balance. A hybrid approach, in which very high resolution modeling (single-tree representation, e.g., Broxton et al., 2015) is used to derive empirical parameters for subgrid parameterization at larger scales, could also be explored.

5.4. Uncertainties, Limitations, and Future Work

Accounting for lidar measurement uncertainty in this type of analysis is difficult, and to the authors' knowledge, has not previously been attempted (e.g., Clemenzi et al., 2018; Deems et al., 2006; Trujillo et al., 2007). For example, addition or subtraction of systematic biases in lidar measurements would not affect analyses of relative snow depth variability and is already explicitly accounted for when bias correcting snow depth maps from snow-free, stable terrain (section 2.3). Alternatively, incorporating perturbations into the snow depth maps to account for a random error would conflict with the assessment of snow depth scaling patterns. Therefore, to examine the potential effects of data uncertainty on our results, we produced an alternative data set at the VH West site (where the influence of shrubs on snow depth is present) by removing all location points whose snow depths were below the raster error calculated there (0.09 m) and compared the results with those obtained with the full data sets. Despite numerical differences, especially in low elevations (see examples in the supporting information), the same scaling behavior can be drawn from both snow depth fields. These findings suggest that any biases of TLS data relative to ALS surveys (as found by Currier et al., 2019) might have a minimal effect on our results within vegetated areas, although we lack the equivalent ALS measurements to fully test this. Further, while small artifacts associated with shrubs may persist in snow depths across VH West, our explicit exclusion of shrub location points makes it unlikely that the systematic bias observed by Currier et al. (2019) would affect our variogram analysis. It should be noted that additional uncertainties arise from the formal detection and characterization of fractals in geophysical variables (e.g., Fleming, 2014; Sun et al., 2006). In particular, the variogram analysis adopted here may introduce errors related to possible overestimation (underestimation) of small (large) fractal dimensions (Wen & Sinding-Larsen, 1997).

In this study, we did not conduct detailed analyses of dependencies between snow depth statistics and terrain parameters (e.g., curvature, terrain roughness), so future efforts should focus on the development of spatially continuous high-resolution DEMs to process other predictors that may feed statistical models for snow depth (e.g., Broxton et al., 2019; Revuelto et al., 2014). Moreover, the results presented here are based on one scan per site during the 2018 snow season, and the corroboration of the interannual consistence reported elsewhere (Clemenzi et al., 2018; Deems et al., 2008; Helfricht et al., 2014; Mendoza, Musselman, et al., 2020; Schirmer & Lehning, 2011) remains a pending task for the extratropical Andes. Finally, a key limitation is the number of AWSs available in Tascadero (only one), and the lack of wind measurements inside the Valle Hermoso experimental catchment, constraining the assessment of wind effects on snow depth scaling patterns in those sites. Future work could take advantage of numerical weather models (e.g., Mott et al., 2011; Mott & Lehning, 2010) to examine the interplay between wind velocity fields, snow depth, vegetation, and topography along the Andes. Further, the combination with physically based models (e.g., Lehning et al., 2006) could help to characterize the relative importance of wind-driven processes (i.e., preferential deposition of snowfall, saltation, suspension, blowing snow sublimation) on observed spatial patterns in snow depth (e.g., Mott et al., 2011) or fully resolved vegetation effects across forested areas like Valle Hermoso (e.g., Harpold et al., 2020).

6. Conclusions

We present the first characterization of snow depth distribution and scaling patterns using terrestrial lidar measurements acquired near maximum snow accumulation dates in 2018, across four hillslopes along the extratropical Andes Cordillera. The dependency of snow depth statistics per elevation band with averaged elevation is examined, and alternative probability functions to represent snow depth variability are tested. Additionally, fractal parameters are obtained from omnidirectional and directional variograms computed for 1-m resolution TLS snow depth maps. The results show that the spatial variability of snow depth is strongly influenced by northness in the sites analyzed and that the relationship with bare earth elevation is site dependent. The lognormal distribution is generally outperformed by either normal or gamma distributions within 25-m elevation bands and the full domains. Moreover, our results confirm not only fractal behavior of snow depth in the Andes—a pattern that has been reported in other mountain regions

worldwide (e.g., Colorado Rockies, Spanish Pyrenees, Swiss Alps)—but also multiscale behavior with up to three distinct fractal regimes. Additional conclusions are as follows:

1. A significant dependence between snow depth and elevation is only found at Las Bayas and the shrub-covered VH West. In nonvegetated areas, snow depth tends to increase up to some threshold elevation, and then decrease at higher elevations.
2. The magnitude of fractal dimensions and omnidirectional scale breaks in snow depth is controlled by local topography and land cover type, rather than average hydroclimatic conditions. Primary omnidirectional breaks (L_1) in unvegetated sites range between 15 and 21 m—in agreement with other mountain ranges worldwide – while L_1 ~4 m in VH west, where small shrubs and a few trees are scattered. Further, fractal dimensions are larger in the latter site at both short and medium ranges, compared to alpine, nonvegetated areas.
3. Secondary scale breaks in snow depth (L_2) are smaller than scale break lengths in bare earth topography, which exhibits fractal behavior up to ~200 m in all sites.
4. In the scanning areas analyzed, the relations between preceding wind direction measurements and anisotropies in bare earth (D) or snow depth fractal parameters (D_S, L_1, L_2) are very site specific.
5. Transect analyses suggest that the magnitude of primary scale breaks in snow depth is related with the mean separation distance "d" between local snow depth peaks. Moreover, the largest average d values in semiarid alpine sites (Tascadero and Las Bayas) are aligned with anisotropies in L_1.

More generally, our results suggest that, along the extratropical Andes, snow depth variability at the hillslope scale is strongly dominated by wind-snow-terrain interactions in the absence of vegetation. Solar radiation exposure and slope are significant controls on snow depth, while elevation shows a weaker overall effect over the scanned domains. Vegetation interactions can only be partially explored given the characteristics of our data set, but the effect of small shrubs can be detected through considerable differences between L_1 and "d" values in alpine versus subalpine sites (VH West).

These findings not only serve as a basis for upcoming investigations on small-scale snowpack dynamics across the extratropical Andes but also provide guidance to design fine-resolution modeling strategies, either statistical or dynamical (i.e., physically-based), and to configure large-scale snow models in mountain environments. Further work is needed to understand the interactions between wind fields, topographic characteristics, vegetation (if existent), and snow deposition/redistribution patterns in the Andes, and lidar technology is expected to play a key role in addressing this challenge.

Appendix A: Detection of Scale Breaks and Fractal Behavior

In this work, we use the same approach as Mendoza, Musselman, et al. (2020) to examine the possibility of different scaling regimes in snow depth and test if fractal behavior exists:

1. Conduct a change point analysis on variograms in the log-log space to find clusters of points sharing a similar trend. We use the E-Divisive non-parametric technique (Matteson & James, 2014), which combines bisection and a divergence measure for multivariate distributions. The change point detection is performed using the "ecp" package (James & Matteson, 2014), implemented in the statistical software "R" (http://www.r-project.org/).
2. Fit linear least squares regression models for variogram points from each group in log-log space (i.e., power laws in raw space), and set intercept estimates as candidate scale break points.
3. Verify whether the changes in the slopes of log-log linear models are larger than 20%, and that 95% confidence limits of the regression slopes do not overlap. If these conditions are satisfied, we conduct a visual inspection of variograms to confirm that the scale break exists, and hence that there is more than one scaling region.
4. Check whether the linear models adjusted in (ii) show $R^2 \geq 0.9$. If this is the case, scaling behavior is described as fractal (Deems et al., 2006, 2008) and the fractal dimension is obtained with Equation 6.

Data Availability Statement

The raw data sets and variogram results for all study sites are available for download at Zenodo (Mendoza, Shaw, et al., 2020 https://doi.org/10.5281/zenodo.3964394).

Acknowledgments

This work was supported by Fondecyt projects 3170079 (P. A. Mendoza), 3180145 (T. E. Shaw, and 1171032 (J. McPhee), and also by the CONICYT/PIA Project AFB180004. We deeply thank Salvador Quezada, Alexis Caro, Felipe Saavedra, Alonso Mejias, Nicole Schaffer, Nicolás Bravo, Jeff Deems, Alex Garcés, Gerardo Zegers, Yohann Videla, Borja Mir, and Luis Marcoleta for their help with collecting these data sets. We thank the La Parva, Valle Nevado, and Valle Hermoso ski resorts for hosting scientific equipment and facilitating our field work. We acknowledge Miguel Lagos for his advice on early versions of this work. Finally, we thank the Associate Editor and two anonymous reviewers for their constructive comments, which greatly helped to improve this manuscript.

References

Alipour, M. H., Rezakhani, A. T., & Shamsai, A. (2016). Seasonal fractal-scaling of floods in two U. S. water resources regions. *Journal of Hydrology*, *540*, 232–239. https://doi.org/10.1016/j.jhydrol.2016.06.016

Antonissen, C. (2018). The effectiveness of a snow fence in the dry Andes region of Chile. Delft University of Technology, Delft, Netherlands.

Arnold, N. S., & Rees, W. G. (2003). Self-similarity in glacier surface characteristics. *Journal of Glaciology*, *49*(167), 547–554. https://doi.org/10.3189/172756503781830368

Ayala, A., McPhee, J., & Vargas, X. (2014). Altitudinal gradients, midwinter melt, and wind effects on snow accumulation in semiarid midlatitude Andes under La Niña conditions. *Water Resources Research*, *50*, 3589–3594. https://doi.org/10.1002/2013WR014960

Blöschl, G. (1999). Scaling issues in snow hydrology. *Hydrological Processes*, *13*(14–15), 2149–2175. https://doi.org/10.1002/(sici)1099-1085(199910)13:14/15<2149::aid-hyp847>3.0.co;2-8

Bozkurt, D., Rojas, M., Boisier, J. P., & Valdivieso, J. (2018). Projected hydroclimate changes over Andean basins in central Chile from downscaled CMIP5 models under the low and high emission scenarios. *Climatic Change*, *150*(3–4), 131–147. https://doi.org/10.1007/s10584-018-2246-7

Broxton, P. D., Harpold, A. A., Biederman, J. A., Troch, P. A., Molotch, N. P., & Brooks, P. D. (2015). Quantifying the effects of vegetation structure on snow accumulation and ablation in mixed-conifer forests. *Ecohydrology*, *8*(6), 1073–1094. https://doi.org/10.1002/eco.1565

Broxton, P. D., van Leeuwen, W. J. D., & Biederman, J. A. (2019). Improving snow water equivalent maps with machine learning of snow survey and lidar measurements. *Water Resources Research*, *55*, 3739–3757. https://doi.org/10.1029/2018WR024146

Clark, M. P., Hendrikx, J., Slater, A. G., Kavetski, D., Anderson, B., Cullen, N. J., et al. (2011). Representing spatial variability of snow water equivalent in hydrologic and land-surface models: A review. *Water Resources Research*, *47*, W07539. https://doi.org/10.1029/2011WR010745

Clemenzi, I., Pellicciotti, F., & Burlando, P. (2018). Snow depth structure, fractal behavior, and interannual consistency over Haut Glacier d'Arolla, Switzerland. *Water Resources Research*, *54*, 7929–7945. https://doi.org/10.1029/2017WR021606

Cornwell, E., Molotch, N. P., & McPhee, J. (2016). Spatio-temporal variability of snow water equivalent in the extra-tropical Andes Cordillera from distributed energy balance modeling and remotely sensed snow cover. *Hydrology and Earth System Sciences*, *20*(1), 411–430. https://doi.org/10.5194/hess-20-411-2016

Cortés, G., Girotto, M., & Margulis, S. (2016). Snow process estimation over the extratropical Andes using a data assimilation framework integrating MERRA data and Landsat imagery. *Water Resources Research*, *52*, 2582–2600. https://doi.org/10.1002/2015WR018376

Cortés, G., & Margulis, S. (2017). Impacts of El Niño and La Niña on interannual snow accumulation in the Andes: Results from a high-resolution 31 year reanalysis. *Geophysical Research Letters*, *44*, 6859–6867. https://doi.org/10.1002/2017GL073826

Currier, W. R., & Lundquist, J. D. (2018). Snow depth variability at the forest edge in multiple climates in the Western United States. *Water Resources Research*, *54*, 8756–8773. https://doi.org/10.1029/2018WR022553

Currier, W. R., Pflug, J., Mazzotti, G., Jonas, T., Deems, J. S., Bormann, K. J., et al. (2019). Comparing aerial lidar observations with terrestrial lidar and snow-probe transects from NASA's 2017 SnowEx campaign. *Water Resources Research*, *55*, 6285–6294. https://doi.org/10.1029/2018WR024533

Deems, J. S., Fassnacht, S. R., & Elder, K. J. (2006). Fractal distribution of snow depth from lidar data. *Journal of Hydrometeorology*, *7*(2), 285–297. https://doi.org/10.1175/JHM487.1

Deems, J. S., Fassnacht, S. R., & Elder, K. J. (2008). Interannual consistency in fractal snow depth patterns at two Colorado mountain sites. *Journal of Hydrometeorology*, *9*(5), 977–988. https://doi.org/10.1175/2008JHM901.1

Deems, J. S., Gadomski, P. J., Vellone, D., Evanczyk, R., LeWinter, A. L., Birkeland, K. W., & Finnegan, D. C. (2015). Mapping starting zone snow depth with a ground-based lidar to assist avalanche control and forecasting. *Cold Regions Science and Technology*, *120*, 197–204. https://doi.org/10.1016/j.coldregions.2015.09.002

Deems, J. S., Painter, T. H., & Finnegan, D. C. (2013). Lidar measurement of snow depth: A review. *Journal of Glaciology*, *59*(215), 467–479. https://doi.org/10.3189/2013JoG12J154

Delignette-Muller, M. L., & Dutang, C. (2015). fitdistrplus: An R package for fitting distributions. *Journal of Statistical Software*, *64*(4), 1–34. https://doi.org/10.18637/jss.v064.i04

Deschamps-Berger, C., Gascoin, S., Berthier, E., Deems, J., Gutmann, E., Dehecq, A., et al. (2020). Snow depth mapping from stereo satellite imagery in mountainous terrain: evaluation using airborne laser-scanning data. *The Cryosphere*, *14*(9), 2925–2940. http://doi.org/10.5194/tc-14-2925-2020

DGA (2017). Metodología para la actualización del balance Hídrico Nacional. Ministerio de Obras Públicas, Dirección General de Aguas, División de Estudios Planificación. Santiago, Chile.

Donald, J. R., Soulis, E. D., Kouwen, N., & Pietroniro, A. (1995). A Land cover-based snow cover representation for distributed hydrologic models. *Water Resources Research*, *31*(4), 995–1009. https://doi.org/10.1029/94WR02973

Escobar, F., & Anabalón, R. (1991). Análisis de las rutas de nieve del país. Dirección General de Aguas, Departamento de Hidrología. Santiago, Chile.

Essery, R., Li, L., & Pomeroy, J. (1999). A distributed model of blowing snow over complex terrain. *Hydrological Processes*, *13*(14–15), 2423–2438. https://doi.org/10.1002/(sici)1099-1085(199910)13:14/15<2423::aid-hyp853>3.0.co;2-u

Fischer, M., Huss, M., Kummert, M., & Hoelzle, M. (2016). Application and validation of long-range terrestrial laser scanning to monitor the mass balance of very small glaciers in the Swiss Alps. *The Cryosphere*, *10*(3), 1279–1295. https://doi.org/10.5194/tc-10-1279-2016

Fleming, S. W. (2014). A non-uniqueness problem in the identification of power-law spectral scaling for hydroclimatic time series. *Hydrological Sciences Journal*, *59*(1), 73–84. https://doi.org/10.1080/02626667.2013.851384

Freudiger, D., Kohn, I., Seibert, J., Stahl, K., & Weiler, M. (2017). Snow redistribution for the hydrological modeling of alpine catchments. *Wiley Interdisciplinary Reviews: Water*, e1232. https://doi.org/10.1002/wat2.1232

Gascoin, S., Lhermitte, S., Kinnard, C., Bortels, K., & Liston, G. E. (2013). Wind effects on snow cover in Pascua-Lama Dry Andes of Chile. *Advances in Water Resources*, *55*, 25–39. https://doi.org/10.1016/j.advwatres.2012.11.013

Glenn, N. F., Spaete, L. P., Sankey, T. T., Derryberry, D. R., Hardegree, S. P., & Mitchell, J. (2011). Errors in LiDAR-derived shrub height and crown area on sloped terrain. *Journal of Arid Environments*, *75*(4), 377–382. https://doi.org/10.1016/j.jaridenv.2010.11.005

Grünewald, T., Bühler, Y., & Lehning, M. (2014). Elevation dependency of mountain snow depth. *The Cryosphere*, *8*(6), 2381–2394. https://doi.org/10.5194/tc-8-2381-2014

Grünewald, T., Schirmer, M., Mott, R., & Lehning, M. (2010). Spatial and temporal variability of snow depth and ablation rates in a small mountain catchment. *The Cryosphere*, *4*(2), 215–225. https://doi.org/10.5194/tc-4-215-2010

Grünewald, T., Stötter, J., Pomeroy, J. W., Dadic, R., Moreno Baños, I., Marturià, J., et al. (2013). Statistical modelling of the snow depth distribution in open alpine terrain. *Hydrology and Earth System Sciences*, *17*(8), 3005–3021. https://doi.org/10.5194/hess-17-3005-2013

Harpold, A. A., Krogh, S. A., Kohler, M., Eckberg, D., Greenberg, J., Sterle, G., & Broxton, P. D. (2020). Increasing the efficacy of forest thinning for snow using high-resolution modeling: A proof of concept in the Lake Tahoe Basin, California, USA. *Ecohydrology*, *13*(4), 1–14. https://doi.org/10.1002/eco.2203

He, S., Ohara, N., & Miller, S. N. (2019). Understanding subgrid variability of snow depth at 1-km scale using lidar measurements. *Hydrological Processes*, *33*(11), 1525–1537. https://doi.org/10.1002/hyp.13415

Hedrick, A. R., Marks, D., Havens, S., Robertson, M., Johnson, M., Sandusky, M., et al. (2018). Direct insertion of NASA airborne snow observatory-derived snow depth time series into the iSnobal energy balance snow model. *Water Resources Research*, *54*, 8045–8063. https://doi.org/10.1029/2018WR023190

Helbig, N., Van Herwijnen, A., Magnusson, J., & Jonas, T. (2015). Fractional snow-covered area parameterization over complex topography. *Hydrology and Earth System Sciences*, *19*(3), 1339–1351. https://doi.org/10.5194/hess-19-1339-2015

Helfricht, K., Schöber, J., Schneider, K., Sailer, R., & Kuhn, M. (2014). Interannual persistence of the seasonal snow cover in a glacierized catchment. *Journal of Glaciology*, *60*(223), 889–904. https://doi.org/10.3189/2014JoG13J197

Huerta, M. L., Molotch, N. P., & McPhee, J. (2019). Snowfall interception in a deciduous Nothofagus forest and implications for spatial snowpack distribution. *Hydrological Processes*, *33*(13), 1818–1834. https://doi.org/10.1002/hyp.13439

Hurst, H. (1951). Long-term storage capacity of reservoirs. *Transactions of the American Society of Civil Engineers*, *116*(1), 770–799.

James, N. A., & Matteson, D. S. (2014). ecp: An R package for nonparametric multiple change point analysis of multivariate data the ecp package. *Journal of Statistical Software*, *62*(7), 1–16. https://doi.org/10.18637/jss.v062.i07

Kirchner, J. W., Feng, X., & Neal, C. (2000). Fractal stream chemistry and its implications for contaminant transport in catchments. *Nature*, *403*, 524–527. https://doi.org/10.1038/35000537

Kirchner, P. B., Bales, R. C., Molotch, N. P., Flanagan, J., & Guo, Q. (2014). LiDAR measurement of seasonal snow accumulation along an elevation gradient in the southern Sierra Nevada, California. *Hydrology and Earth System Sciences*, *18*(10), 4261–4275. https://doi.org/10.5194/hess-18-4261-2014

Korres, W., Reichenau, T. G., Fiener, P., Koyama, C. N., Bogena, H. R., Cornelissen, T., et al. (2015). Spatio-temporal soil moisture patterns – A meta-analysis using plot to catchment scale data. *Journal of Hydrology*, *520*, 326–341. https://doi.org/10.1016/j.jhydrol.2014.11.042

Kuchment, L. S., & Gelfan, A. N. (1996). The determination of the snowmelt rate and the meltwater outflow from a snowpack for modelling river runoff generation. *Journal of Hydrology*, *179*(1–4), 23–36. https://doi.org/10.1016/0022-1694(95)02878-1

Kuchment, L. S., & Gelfan, A. N. (2007). Statistical self-similarity of spatial variations of snow cover and its application for modelling snowmelt runoff generation in basins with a sparse snow measurement network. In *Predictions in ungauged basins: PUB kick-off* (pp. 156–163), Brasilia. IAHS Publications.

Lehning, M., Völksch, I., Gustafsson, D., Nguyen, T. A., Stähli, M., & Zappa, M. (2006). ALPINE3D: A detailed model of mountain surface processes and its application to snow hydrology. *Hydrological Processes*, *20*(10), 2111–2128. https://doi.org/10.1002/hyp.6204

Li, L., & Pomeroy, J. W. (1997). Estimates of threshold wind speeds for snow transport using meteorological data. *Journal of Applied Meteorology*, *36*(3), 205–213. https://doi.org/10.1175/1520-0450(1997)036<0205:eotwsf>2.0.co;2

Liston, G. E. (1999). Interrelationships among snow distribution, snowmelt, and snow cover depletion: Implications for atmospheric, hydrologic, and ecologic modeling. *Journal of Applied Meteorology*, *38*(10), 1474–1487. https://doi.org/10.1175/1520-0450(1999)038<1474:iasdsa>2.0.co;2

Liston, G. E. (2004). Representing subgrid snow cover heterogeneities in regional and global models. *Journal of Climate*, *17*(6), 1381–1397. https://doi.org/10.1175/1520-0442(2004)017<1381:rsschi>2.0.co;2

Liston, G. E., & Elder, K. (2006). A distributed snow-evolution modeling system (snowmodel). *Journal of Hydrometeorology*, *7*(6), 1259–1276. https://doi.org/10.1175/JHM548.1

López-Moreno, J. I., Fassnacht, S. R., Heath, J. T., Musselman, K. N., Revuelto, J., Latron, J., et al. (2013). Small scale spatial variability of snow density and depth over complex alpine terrain: Implications for estimating snow water equivalent. *Advances in Water Resources*, *55*, 40–52. https://doi.org/10.1016/j.advwatres.2012.08.010

López-Moreno, J. I., Revuelto, J., Fassnacht, S. R., Azorín-Molina, C., Vicente-Serrano, S. M., Morán-Tejeda, E., & Sexstone, G. A. (2015). Snowpack variability across various spatio-temporal resolutions. *Hydrological Processes*, *29*(6), 1213–1224. https://doi.org/10.1002/hyp.10245

Luce, C. H., & Tarboton, D. G. (2004). The application of depletion curves for parameterization of subgrid variability of snow. *Hydrological Processes*, *18*(8), 1409–1422. https://doi.org/10.1002/hyp.1420

Mandelbrot, B. B. (1982). *The fractal geometry of nature*. San Francisco: W. H. Freeman and Co.

Mandelbrot, B. B. (1988). An introduction to multifractal distribution functions. In *Random fluctuations and pattern growth: Experiments and models* (pp. 279–291). Dordrecht: Springer.

Mandelbrot, B. B., & Wallis, J. R. (1968). Noah, Joseph and operational hydrology. *Water Resources Research*, *4*(5), 909–918. https://doi.org/10.1029/WR004i005p00909

Marchand, W.-D., & Killingtveit, A. (2005). Statistical probability distribution of snow depth at the model sub-grid cell spatial scale. *Hydrological Processes*, *19*(2), 355–369. https://doi.org/10.1002/hyp.5543

Mark, D. M., & Aronson, P. B. (1984). Scale-dependent fractal dimensions of topographic surfaces: An empirical investigation, with applications in geomorphology and computer mapping. *Mathematical Geology*, *16*(7), 671–683. https://doi.org/10.1007/bf01033029

Marshall, A. M., Link, T. E., Abatzoglou, J. T., Flerchinger, G. N., Marks, D. G., & Tedrow, L. (2019). Warming alters hydrologic heterogeneity: Simulated climate sensitivity of hydrology-based microrefugia in the snow-to-rain transition zone. *Water Resources Research*, *55*, 2122–2141. https://doi.org/10.1029/2018WR023063

Masiokas, M. H., Rabatel, A., Rivera, A., Ruiz, L., Pitte, P., Ceballos, J. L., et al. (2020). A review of the current state and recent changes of the Andean cryosphere. *Frontiers in Earth Science*, *8*, 1–27. https://doi.org/10.3389/feart.2020.00099

Masiokas, M. H., Villalba, R., Luckman, B. H., le Quesne, C., & Aravena, J. C. (2006). Snowpack variations in the Central Andes of Argentina and Chile, 1951–2005: Large-scale atmospheric influences and implications for water resources in the region. *Journal of Climate*, *19*, 6334–6352. https://doi.org/10.1175/JCLI3969.1

Matteson, D. S., & James, N. A. (2014). A nonparametric approach for multiple change point analysis of multivariate data. *Journal of the American Statistical Association*, *109*(505), 334–345. https://doi.org/10.1080/01621459.2013.849605

Melvold, K., & Skaugen, T. (2013). Multiscale spatial variability of lidar-derived and modeled snow depth on Hardangervidda, Norway. *Annals of Glaciology*, *54*(62), 273–281. https://doi.org/10.3189/2013AoG62A161

Mendoza, P., Shaw, T., McPhee, J., Musselman, K., Revuelto, J., & MacDonell, S. (2020). *Lidar-derived snow depth maps along the Chilean Extratropical Andes, winter 2018*. https://doi.org/10.5281/zenodo.3964394

Mendoza, P. A., Musselman, K. N., Revuelto, J., Deems, J. S., López-Moreno, J. I., & McPhee, J. (2020). Interannual and seasonal variability of snow depth scaling behavior in a subalpine catchment. *Water Resources Research*, *56*, e2020WR027343. https://doi.org/10.1029/2020WR027343

Mendoza, P. A., Rajagopalan, B., Clark, M. P., Cortés, G., & McPhee, J. (2014). A robust multimodel framework for ensemble seasonal hydroclimatic forecasts. *Water Resources Research*, *50*, 6030–6052. https://doi.org/10.1002/2014WR015426

Mernild, S. H., Liston, G. E., Hiemstra, C. A., Malmros, J. K., Yde, J. C., & McPhee, J. (2017). The Andes Cordillera. Part I: Snow distribution, properties, and trends (1979-2014). *International Journal of Climatology*, *37*(4), 1680–1698. https://doi.org/10.1002/joc.4804

Mott, R., & Lehning, M. (2010). Meteorological modeling of very high-resolution wind fields and snow deposition for mountains. *Journal of Hydrometeorology*, *11*(4), 934–949. https://doi.org/10.1175/2010JHM1216.1

Mott, R., Schirmer, M., & Lehning, M. (2011). Scaling properties of wind and snow depth distribution in an Alpine catchment. *Journal of Geophysical Research*, *116*, D06106. https://doi.org/10.1029/2010JD014886

Musselman, K. N., Pomeroy, J. W., Essery, R. L. H., & Leroux, N. (2015). Impact of windflow calculations on simulations of alpine snow accumulation redistribution and ablation. *Hydrological Processes*, *29*(18), 3983–3999. https://doi.org/10.1002/hyp.10595

Olsson, J., Niemczynowicz, J., & Berndtsson, R. (1993). Fractal analysis of high-resolution rainfall time series. *Journal of Geophysical Research*, *98*(D12), 23265. https://doi.org/10.1029/93JD02658

Painter, T. H., Berisford, D. F., Boardman, J. W., Bormann, K. J., Deems, J. S., Gehrke, F., et al. (2016). The Airborne Snow Observatory: Fusion of scanning lidar, imaging spectrometer, and physically-based modeling for mapping snow water equivalent and snow albedo. *Remote Sensing of Environment*, *184*, 139–152. https://doi.org/10.1016/j.rse.2016.06.018

Pebesma, E. J. (2004). Multivariable geostatistics in S: The gstat package. *Computers and Geosciences*, *30*(7), 683–691. https://doi.org/10.1016/j.cageo.2004.03.012

Revuelto, J., López-Moreno, J. I., Azorin-Molina, C., & Vicente-Serrano, S. M. (2014). Topographic control of snowpack distribution in a small catchment in the central Spanish Pyrenees: Intra- and inter-annual persistence. *The Cryosphere*, *8*(5), 1989–2006. https://doi.org/10.5194/tc-8-1989-2014

Schirmer, M., & Lehning, M. (2011). Persistence in intra-annual snow depth distribution: 2. Fractal analysis of snow depth development. *Water Resources Research*, *47*, W09517. https://doi.org/10.1029/2010WR009429

Schirmer, M., Wirz, V., Clifton, A., & Lehning, M. (2011). Persistence in intra-annual snow depth distribution: 1. Measurements and topographic control. *Water Resources Research*, *47*, 1–16. https://doi.org/10.1029/2010WR009426

Shaw, T. E., Gascoin, S., Mendoza, P. A., Pellicciotti, F., & McPhee, J. (2020). Snow depth patterns in a high mountain Andean catchment from satellite optical tristereoscopic remote sensing. *Water Resources Research*, *56*, e2019WR024880. https://doi.org/10.1029/2019WR024880

Shook, K., & Gray, D. (1996). Small-scale spatial structure of spatial snowcovers. *Hydrological Processes*, *10*(10), 1283–1292. https://doi.org/10.1002/(sici)1099-1085(199610)10:10<1283::aid-hyp460>3.0.co;2-m

Skaugen, T., & Melvold, K. (2019). Modeling the snow depth variability with a high-resolution lidar data set and nonlinear terrain dependency. *Water Resources Research*, *55*, 9689–9704. https://doi.org/10.1029/2019WR025030

Skaugen, T., & Weltzien, I. H. (2016). A model for the spatial distribution of snow water equivalent parameterized from the spatial variability of precipitation. *The Cryosphere*, *10*(5), 1947–1963. https://doi.org/10.5194/tc-10-1947-2016

Sun, W., Xu, G., Gong, P., & Liang, S. (2006). Fractal analysis of remotely sensed images: A review of methods and applications. *International Journal of Remote Sensing*, *27*(22), 4963–4990. https://doi.org/10.1080/01431160600676695

Swenson, S. C., Clark, M., Fan, Y., Lawrence, D. M., & Perket, J. (2019). Representing intrahillslope lateral subsurface flow in the community land model. *Journal of Advances in Modeling Earth Systems*, *11*, 4044–4065. https://doi.org/10.1029/2019MS001833

Planet Team (2018). Planet application program interface. In *Space for life on Earth*. San Francisco, CA, USA. Retrieved from www.planet.com

Trujillo, E., Ramírez, J. A., & Elder, K. J. (2007). Topographic, meteorologic, and canopy controls on the scaling characteristics of the spatial distribution of snow depth fields. *Water Resources Research*, *43*, W07409. https://doi.org/10.1029/2006WR005317

Trujillo, E., Ramírez, J. A., & Elder, K. J. (2009). Scaling properties and spatial organization of snow depth fields in sub-alpine forest and alpine tundra. *Hydrological Processes*, *23*(11), 1575–1590. https://doi.org/10.1002/hyp.7270

Veitinger, J., Sovilla, B., & Purves, R. S. (2014). Influence of snow depth distribution on surface roughness in alpine terrain: A multi-scale approach. *The Cryosphere*, *8*(2), 547–569. https://doi.org/10.5194/tc-8-547-2014

Wen, R., & Sinding-Larsen, R. (1997). Uncertainty in fractal dimension estimated from power spectra and variograms. *Mathematical Geology*, *29*(6), 727–753. https://doi.org/10.1007/BF02768900

Wilks, D. S. (2011). *Statistical methods in the atmospheric sciences* (3rd ed.). Academic Press.

Winstral, A., & Marks, D. (2014). Long-term snow distribution observations in a mountain catchment: Assessing variability, time stability, and the representativeness of an index site. *Water Resources Research*, *50*, 293–305. https://doi.org/10.1002/2012WR013038

Xu, C., Li, Z., Li, H., Wang, F., & Zhou, P. (2018). Long-range terrestrial laser scanning measurements of summer and annual mass balances for Urumqi Glacier No. 1, eastern Tien Shan, China. *The Cryosphere Discussions*, 1–28. https://doi.org/10.5194/tc-2018-128

Xu, C., McDowell, N. G., Fisher, R. A., Wei, L., Sevanto, S., Christoffersen, B. O., et al. (2019). Increasing impacts of extreme droughts on vegetation productivity under climate change. *Nature Climate Change*, *9*(12), 948–953. https://doi.org/10.1038/s41558-019-0630-6

Yates, F. (1948). Systematic sampling. *Philosophical Transactions of the Royal Society of London Series A, Mathematical and Physical Sciences*, *241*(834), 345–377. https://doi.org/10.1098/rsta.1948.0023

Zheng, Z., Kirchner, P. B., & Bales, R. C. (2016). Topographic and vegetation effects on snow accumulation in the southern Sierra Nevada: a statistical summary from lidar data. *The Cryosphere*, *10*(1), 257–269. https://doi.org/10.5194/tc-10-257-2016